Merseburg University of Applied Sciences

Department of Engineering and Natural Sciences

Program: Chemical and Environmental Engineering

Synthesis and immobilization of modified Ruthenium(II)-pyrithione complexes on mesoporous nanostructured silica

Masterthesis

For attaining the academic degree

Master of Engineering (M.Eng)

Submitted by

Florian Max Dietrich

First Referee: Prof. Dr. Dr. h.c. Goran Kaluđerović

Second Referee: Prof. Dr. Iztok Turel

Acknowledgement

First, I would like to thank my thesis advisors Prof. Dr. Dr. h.c. Goran Kaluđerović and Prof. Dr. Iztok Turel for the unique possibility to work on this research topic as part of the “DAAD HAW” project in their research groups at University of Applied Sciences Merseburg and University of Ljubljana. I am extremely grateful for the continuous supervision, support and advise as well as for reading and revising my thesis, guiding this work in the right direction.

In addition, I would like to thank my supervisors in each working group M.Eng. T. Becker and M.Sc. U. Rapuš for their mentorship. Without their expertise and constant patience, guidance and support throughout my research work this thesis would not have been possible.

I would further like to thank Mrs. S. Wusterhausen, Dipl. Ing. O. Krimig and Dipl. Ing. T. Stam-Creutz for their support in terms of experimental work as well as BET and SEM measurements at University of Applied Sciences Merseburg.

Special thanks apply to the working groups at University of Applied Sciences Merseburg and University of Ljubljana for their sincere welcome, support and the inspirational atmosphere.

Finally, I would like to express my profound gratitude to my family, especially my mother and sister, for their invaluable support and encouragement during my studies. Without them this accomplishment would not have been achieved.

Statement of Authorship

I hereby declare that I wrote this master thesis by myself without unauthorized external assistance, unless otherwise acknowledged in the text. All verbatim and referenced passages and all sources of information have been quoted and indicated.

This thesis has not been submitted for any other degree.

Merseburg, the 20th of August 2024

_____

Florian Dietrich

Table of contents

List of tables and figures

List of Tables:

List of Schemes:

List of Figures:

List of Figures in Appendix:

List of Abbreviations

DNA	Deoxyribonucleic acid
Cisplatin	*cis*-Diamminedichloridoplatinum(II)
MSNs	Mesoporous silica nanoparticles
MCM-41	Mobile Composition of Matter No. 41
SBA-15	Santa Barbara Amorphous No. 15
SDA	Structure-directing agent
TEOS	Tetraethyl orthosilicate
PZC	Point of zero charge
CTAB	Cetyltrimethylammonium bromide
Pluronic® P123	Polyethylene(oxide)-polypropylene(oxide)-Polyethylene(oxide) triblock copolymer
PEG	Poly(ethyleneglycol)
EPR-effect	Enhanced permeability and retention effect
Pyrithione	1-Hydroxy-2(1*H*)-pyridinethione
Zinc-pyrithione	*bis*-(2-mercaptopyridine-*N*-oxide)zinc(II)
CMR-substance	carcinogenic, germ-cell mutagenic and reprotoxic substance
HSV	Herpes simplex virus
THA	Tetrahydroanthracen
p-cym	1-Methyl-4-(propan-2-yl)benzene
AKR1C	Aldo-keto reductase subfamily 1C
Ru(II)-pyrithione	[(η^6-*p*-cym)Ru(1-hydroxidopyridine-2(1*H*)-thionato)Cl]
GSTs	Glutathione-*S*-transferases
ROS	Reactive oxygen species
RGD-sequence	Arginine-glycine-aspartic acid peptide sequence
NMR spectroscopy	Nuclear magnetic resonance spectroscopy

ESI-MS	Electrospray ionisation mass spectrometry
EA	Elemental analysis
BET	Low temperature N_2-sorption Analysis using Brunauer-Emmett-Teller method
SEM	Scanning electron microscopy
DLS	Dynamic light scattering
EDAX	Energy dispersive X-ray spectroscopy
HL1	1-Hydroxy-2(1*H*)-pyridinethione
H_2L2	1-Hydroxy-2-thioxo-1,2-dihydropyridine-3-carboxylic acid
HL3	Ethyl 1-hydroxy-2-thioxo-1,2-dihydropyridine-3-carboxylate
M2CN	Methyl-2-chloronicotinate
I1	2-chloro-3-(methoxycarbonyl)-pyridine-N-oxide
UHP	Urea-hydrogenperoxide
TFAA	Trifluoroacetic anhydride
DCM	Dichloromethane
NaOMe	Sodium Methoxide
[{Ru(*p*-cymene)Cl_2}$_2$]	Dichloro-(*p*-cymene)ruthenium(II) dimer
1	[(η^6-*p*-cym)Ru(**L1**)Cl]
2	[(η^6-*p*-cym)Ru(**HL2**)Cl]
3	[(η^6-*p*-cymRu(**L3**)Cl]
IUPAC	International Union of Pure and Applied Chemistry
BJH	Barret, Joyner and Halenda
w%	Weight-percent

Abstract

Since the discovery of first anticancer drug, cisplatin, in the late 1960´s the importance of chemotherapeutics is rising constantly. However, problems of commonly used platinum-based drugs like low bioavailability, severe side-effects and drug resistance towards several cancers limit the application of established anticancer agents, thus requiring further research for more efficient and safe alternatives. Organoruthenium(II) complexes have proven to provide high bioactivity towards malignant cells, making them prominent candidates for alternative anticancer drugs. Especially when bound to arene ligands like *p*-cymene they provide enhanced stability in aqueous solutions as well as less toxicity towards normal cells compared to platinum-based drugs. Their cytotoxicity could further be enhanced if pyrithione ligands are bonded to ruthenium(II). To overcome still present drawbacks of these complexes (e.g., complex hydrolysis), the usage of drug delivery systems could lead to improved bioavailability and selectivity. Mesoporous silica nanostructures (MSNs) provide high surface area and good biocompatibility, thus being prominent candidates for the use as carrier systems. Regarding the enhanced accumulation of MSNs in tumour tissues due to the EPR-effect, loading of transition-metal drugs into mesoporous nanostructured silica is likely to increase the bioavailability and selectivity of anticancer drugs, leading to lower doses required.

Within this work the three (*p*-cymene)ruthenium(II) pyrithione compounds **1–3** were successfully synthesized and characterized by IR and multinuclear NMR spectroscopy and purity was also confirmed by elemental analysis. Evaluation of the prepared complexes revealed a novel coordination mode of the carboxylate pyrithione derivative **HL2**$^{-}$ when bonded to the ruthenium(II) central ion, assuming that coordination in compound **2** takes place via thione sulphur and the carboxylate oxygen atoms. However, this presumption has to be further verified by X-ray structural analysis.

Mesoporous nanostructured silica particles MCM-41 and SBA-15 were synthesized and further characterized using SEM, DLS and BET-analysis, showing size, shape and surface area sufficient for drug loading. Subsequently complexes **1–3** were successfully loaded into prepared MSNs, revealing ruthenium contents of 21.0–27.0 *w*% with EDX-analysis. Loading efficiencies of used compounds vary between 57.0–90.4 %, showing highest values for complex **1** due to less bulky ligand substitutes. Furthermore, a tendency of increased adsorption of all compounds into MCM-41 was observed. Nanomaterials remained without alterations in shape and morphology upon immobilization.

Obtained results reveal successful preparation of loaded nanostructures with organoruthenium(II) complexes MCM-41|**1–3** and SBA-15|**1–3** thus highlighting their potential use for subsequent biological studies towards tumour cells.

1 Introduction

1.1 General Introduction

In 1965 *Barnett Rosenberg* discovered the inhibiting effect of *cis*-diamminedichloridoplatinum(II) (cisplatin), investigating a stagnation in cell division of *E. coli* while generating an electric field within the bacteria chamber.[1] The examination of the experiment stated that not the electric field, but the formation of cisplatin due to the usage of platinum electrodes in ammonium chloride buffer solution is responsible for the inhibition.[1] This discovery is considered as the birth of medicinal inorganic chemistry.[2] After demonstrating that cisplatin is able to inhibit growth of sarcoma 180 and leukaemia 1210 cancer lines in mice[3] as well as showing excellent results in preclinical pharmacology and toxicology tests, the compound was finally approved for testicular and ovarian cancer therapy by the U.S. Food and Drug Administration in 1978.[2,4] A variety of research methods showed that cisplatin interacts with deoxyribonucleic acid (DNA) which is crucial for its activity.[5–7] The cross-linking with DNA causes irreversible damage preventing DNA replication of the tumour cells and further leading to apoptosis.[4,8] Despite providing high cytotoxicity the interaction of cisplatin with healthy tissues shows many side-effects such as nephrotoxicity[9], nausea and vomiting.[10] However, the biggest drawback is the resistance of several cancers against cisplatin reported in various studies.[11–13] Therefore, the development of novel metal-based antitumour drugs is crucial. Besides platinum based compounds, organoruthenium(II) complexes have turned out to be one of the most promising contender of alternative anticancer agents[14] showing advantages in terms of stability, cancer resistance and less severe side effects.[15–18]

However, the disadvantages of currently used chemotherapeutics such as their low bioavailability and the severe side-effects accompanying anticancer therapy make it impossible to cure cancer without permanent impairments up to today.[2] As recently reported, the bioavailability of anticancer drugs can be enhanced due to higher solubility and protection against biodegradation when using nanoparticles as a drug delivery system.[19,20] Mesoporous silica nanostructures (MSNs) are suiting the demands for this purpose the best. Most commonly used (*in vitro*) MSNs types are SBA-15 and MCM-41 particles exhibiting hexagonally ordered pores with specific surface areas up to 1000 $\mathrm{m}^2 \cdot \mathrm{g}^{-1}$. [21,22] Due to their nontoxic behaviour and biocompatibility the utilization of drug-loaded MSNs of this type showed mostly enhanced antitumor activity in comparison to free drugs.[23,24]

1.2 Mesoporous nanostructured silica

Due to their unique physicochemical properties such as high specific surface area, large pore volume, adjustable pore size and the ability of simple functionalization, mesoporous silica nanoparticles have emerged as promising drug delivery system.[19,25] Providing a precise particle size and shape as well as a high biocompatibility, MSNs have come to great interest as carrier system especially for anticancer drugs.[19,25]

The commonly used synthesis route for preparing MSNs such as MCM-41 and SBA-15 is a sol-gel process using a modified Stöber synthesis involving the formation of a silica network through hydrolysis and condensation of a silica precursor in the presence of a structure-directing agent (SDA).[19,25] As shown in Figure 1, in the first step the SDA has to be dissolved in pure water, forming single spherical micelles which arrange in hexagonal assemblies further.[19,20] Subsequently the silica precursor, typically tetraethyl orthosilicate (TEOS), is added to the solution. The silica network is then formed by acidic or basic catalyzed hydrolysis and condensation reactions.[19,26] The point of zero charge (PZC), where Si-OH containing species are present without charge, ranges between pH 2–3 depending on the degree of condensation. Present pH values above three thus result in condensation reactions through basic catalysis, whereas condensation in pH values below two is induced via acid catalysis.[19,26] Since the interaction between the surfactant template and the resulting material is important, surfactants used as SDA are highly depending on the present milieu.[19] Due to the fact that silica species are present negatively charged in alkaline conditions (pH > 3), the utilization of cationic surfactants such as cetyltrimethylammonium bromide (CTAB) is suitable for basic catalyzed reactions (e.g., MCM-41).[19,26] The use of acidic conditions leads to opposing tensides.[19] Procedures using milieus within the PZC (2 < pH < 3; e.g., SBA-15) require anionic surfactants for instance blockpolymers such as Pluronic® P123.[19,26] The certain size and shape of the pores and particles can be defined during the hydrolysation and condensation step adjusting micelle concentration, temperature, pH-value and stirring speed of the solution.[19,20,25] To obtain a biocompatible product, the surfactant has to be removed after the complete formation of a solid silica structure, using washing and calcination processes.[19,20,25] Overall, the sol-gel synthesis method provides a reliable process for the production of mesoporous silica particles with well-defined pore structures and high surface areas with varying sizes between 20 nm up to 1000 nm. [19,20]

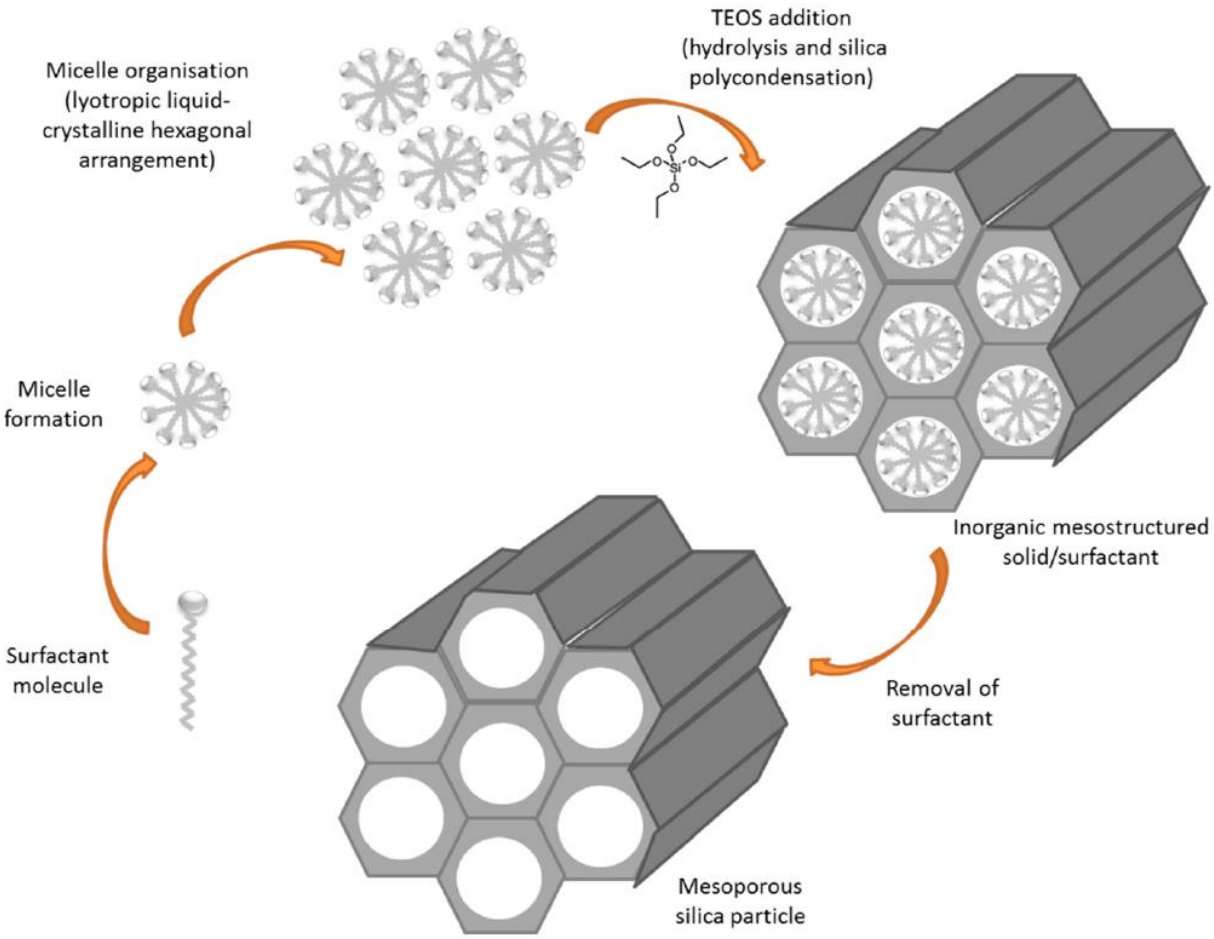

Figure 1: Schematic synthesis of mesoporous silica nanoparticles[20]

Upon introduction into biological systems, MSNs interact with cellular membranes and are primarily internalized by cells through different ways of endocytosis.[25] All processes involve the enclosure of nanoparticles by the cell membrane, forming vesicles that transport the MSNs into the cytoplasm where they are further delivered to endosomes, late endosomes and lysosomes.[25,27] For the study of particles a simplified classification is generally used, categorizing endocytic pathways into four types: clathrin-mediated endocytosis, caveolae-mediated endocytosis, macropinocytosis, and clathrin-independent/caveolae-independent pathways.[25,27] However, the most prominent route of uptake into the cell is clathrin-dependent endocytosis.[27] Mediated by receptors, the particles are taken up by clathrin-coated pits, leading to vesicles, which are further processed to endosomes. The degradation of the particles is mediated via lysosomes proceeding to the formation of orthosilicic acid ($Si(OH)_4$), beneficial for humans, and the release of potentially encapsulated compounds.[25,27,28] Evaluating the interaction of MSNs in biological systems, the particle size is suggested to play an important role either. The examination of size dependent haemolytic activity of MCM-41 particles states that nanoparticles with smaller diameter tend to exhibit higher haemolytic activity.[29] Furthermore well-ordered pore structures have a tendency of reduced interactions with red

blood cells as well as the surface functionalization with poly(ethyleneglycol) (PEG), leading to lower haemolytic activity.[29] Investigating the *in vivo* biodistribution and urinary excretion of MSNs with particle sizes of 80, 120, 200 and 360 nm, *He, Zhang et al.* discovered that large particles more likely accumulate in organs such as liver and spleen, whereas smaller particles tend to have a higher biodistribution due to a longer blood-circulation lifetime, respectively.[30] However, smaller particles show a lower degradation time compared to larger ones, whereas none of the test animals showed abnormalities due to treatment with MSNs.[30] The relatively low cytotoxicity is observed in similar *in vivo* studies too. The biocompatibility and -distribution of MSNs as well as their drug delivery efficiency for instance was investigated by *Lu et al.* injecting doses of 50 $\mathrm{mg \cdot kg^{-1}}$ nanoparticles intravenously in mice twice per week for 14 days, resulting in just mildly elevated levels of liver transaminase in one out of two mice.[31] Same dosage was applied intraperitoneal twice per week for two months, showing no unusual responses or behaviours as well as normal ranges of measured factors in haematology results, therefore indicating no inflammatory reaction due to long term treatment.[31] The excretion of 94.4 % of all injected amount of silicon through urine and faeces within four days is most likely a contributing factor to the low toxicity observed.[31] While comparable results on the accumulation of MSNs in liver and spleen were highlighted,[30] the study additionally shows the preferential concentration in tumour sites, emphasising the potential use of nanoparticles as a delivery system for anticancer drugs.[31] Nevertheless, their uptake and circulation *in vivo* needs to be further investigated, particularly with regard to the effects of particle size, shape and surface area.

The inhibitory effect of currently used chemotherapeutics is mostly limited because of their low solubility and stability in aqueous solutions, requiring high dosages thus provoking severe side-effects[19]. Providing good bioavailability and biocompatibility, MSNs are beneficial for the usage as drug-carrier systems to overcome these issues. The immobilization of anticancer drugs into mesoporous silica species is likely to protect them from decomposition meanwhile elevating their solubility.[32] Various references are evaluating the possibility of loaded MSNs enhancing chemotherapy, improving transport and selectivity of utilized drugs.[19, 20, 31] Precisely interacting with tumour tissues, MSNs can target specific cells either passive or active. Passive targeting is mainly functioning due to the so-called enhanced permeability and retention effect (EPR-effect).[20] Showing clear differences to healthy tissue, solid tumour tissue exhibits increased vascular permeability due to the abnormal development of blood vessels thus offering particles or other macromolecules to diffuse into malignant tissue more easily.[19] Additionally, the elution through blood vessels and moreover the subsequent removal by the lymphatic system proceeds slower in tumour tissue compared to healthy tissue.[19] Whereas the pore cut-off size

in healthy tissue ranges between 4 – 25 nm, the maximum vascular pore size of tumours blood vessels can vary between 380 – 780 nm.[20] Regarding the rapid elution of particles with diameters less than 80 nm as well, the optimal particle size for passive accumulation of MSNs in tumours can vary from 80 – 200 nm.[19] However, the accumulation of particles in circulating malignant cells such as leukaemia or metastasised cells is not possible via EPR-effect.[19] Active targeting, on the other hand, refers to differing types and numbers of surface receptors in malignant cells compared to healthy tissue.[19,20] Due to their high proliferation tendency, thus resulting in an increased need of energy, cancer cells possess a higher number of glucose or folate receptors on the cell surface. The functionalization of MSNs using surface ligands which are able to bind on these receptors (e.g., sugar molecules, folic acid, aptamers or antibodies), could lead to an increased interaction with targeted cells thus achieving a higher selectivity.[19,20]

Evaluating the effect of drug loaded MSNs *in vitro* and *in vivo*, it was shown that the efficiency of cancer inhibiting compounds might be improved through increased accumulation in tumours.[23,31,33] Considering the abilities of drug loaded nanostructured mesoporous silica to accumulate preferably in solid tumour sites without severe toxic side-effects as well as the possibility of surface-functionalization to enhance the selectivity and accumulation in malignant cells described previously, MSNs seem to be one of the most prominent candidates for overcoming major problems of current anticancer therapy.

1.3 Pyrithione-based ruthenium(II) complexes

1.3.1 Pyrithione based metal ionophores

Allium Stipitatum, also known as “Persian shallot”, is one of the most used alliaceous species in Iran, Turkey and Central Asia.[34] Known for its antimicrobial and anti-inflammatory properties, it is commonly used in traditional Iranian folk medicine for the treatment of rheumatic and inflammatory disorders such as gout, arthritis or diarrhoea.[34] Containing various organosulphur compounds, it was found that especially the presence of 1-hydroxy-2(1*H*)-pyridinethione (pyrithione) is responsible for providing these medical effects.[34] Pyrithione is a sulphur containing pyridine-*N*-oxide, in solution present as a mixture of two tautomeric species (Figure 2).[35] Providing antifungal and antimicrobial properties, it is widely used as the metal complex *bis*-(2-mercaptopyridine-*N*-oxide)zinc(II) (zinc-pyrithione) in over the counter treatments for dandruff and seborrheic dermatitis or as well used as industrial biocide.[36] Although zinc-pyrithione is considered safe for use in anti-dandruff shampoos in concentrations of up to 1%, it was banned by the European Union in 2021 due to its reclassification as CMR-substance of class 1B.[37,38]

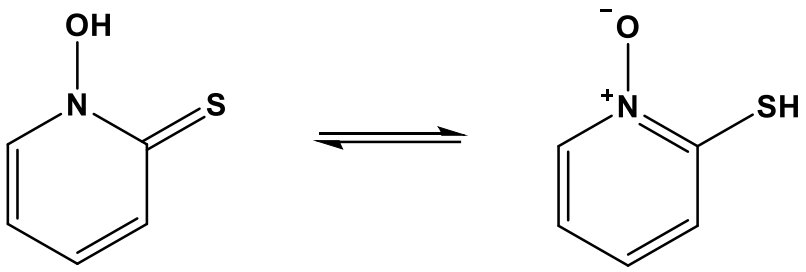

*Figure 2: Tautomer forms of pyrithione (**HL1**)*

The biological activity of pyrithione metal complexes can be explained by means of their acting as metal ionophores. Diffusing through the cell membrane, the uncharged pyrithione molecule ionises intracellularly thereby collapsing a transmembrane pH driving force.[35] Pyrithione itself hence serves as proton conductor.[35] Thus inducing enhanced transportation and transfer of metal ions through bimolecular lipid membranes, pyrithione metal complexes such as zinc-pyrithione cause an increase of intracellular metal-ion concentration of bound metals, in this case Zn^{2+}.[39,40] For instance, it was found that the replication of herpes simplex virus (HSV) is inhibited when exposed to zinc-pyrithione complex.[41] Facilitating the transport of Zn^{2+} ions into the cells, zinc-pyrithione disrupts the activation of the NF-κB pathway necessary for HSV replication and proliferation.[41] Additionally it can be stated that zinc-pyrithione induces apoptosis in Hep-2 cervical tumour cells due to the elevation of intracellular Zn^{2+} levels.[42] The bioactivity of zinc-pyrithione has been demonstrated in several studies, showing that the biological effects result predominantly due to the increase in intracellular Zn^{2+} levels caused by the function of the pyrithione ligand as an ionophore.[35,40–42] Interestingly, it was also recently reported that zinc-pyrithione is a potent inhibitor of PL^{Pro} and cathepsin L enzymes with *ex vivo* inhibition of SARS-CoV-2 entry and replication.[43] Regarding these results, the use of pyrithione as a ligand in organometallic complexes comes to great interest providing the ability of transferring metal ions through cell membranes enhancing the intracellular concentration of bioactive metal ions.

1.3.2 Organometallic ruthenium(II) complexes

The usage of organometallic complexes in medicinal applications especially for anticancer therapy is constantly rising since cisplatin and its derivatives are widely used as drugs for chemotherapeutical treatments. Showing great results for inhibiting the growth of malignant tissue, the biomedical properties of platinum(II) metal complexes are beyond all question. Nevertheless, therapy with common platinum(II) based drugs is accompanied with several disadvantages as well.[11] Due to the severe side-effects caused by conventional chemotherapeutics and the resistance that may be developed by some cancers upon

treatment, there is significant interest in discovering novel metal-based compounds which can have different mechanism of action compared to platinum-based drugs. One of the most promising candidates for the substitution of platinum in anticancer agents is ruthenium.[14] Found in the same group as iron, ruthenium is a transition metal belonging to the so-called platinum group elements.[44] It is used in the field of cancer research mostly in its oxidation states ruthenium(II) and ruthenium(III) due to the versatile coordination chemistry.[14] Forming a variety of stable coordinations, including organometallic complexes as well as providing similar stability and ligand exchange kinetics as common platinum-based drugs, ruthenium(II) and ruthenium(III) compounds have garnered attention for their potential as chemotherapeutic agents, whereas the reduced form is considered to be more active.[14,45] Despite of some similarities to platinum(II) compounds, organoruthenium complexes offer several advantages in terms of bioavailability and biotoxicity.

In general ruthenium compounds are considered less toxic than platinum-based drugs due to their high selectivity towards tumours and thus less severe side-effects.[45] The decreased toxicity is believed to derive from the ability of ruthenium to mimic iron in binding to many biomolecules although not all authors support this comparison.[45,46] Similar as iron, ruthenium is able to interact with serum transferrin and albumin, which are used to transport iron ions throughout the organism.[47] As a result of enhanced proliferation, tumour tissues require a higher amount of iron leading to an increased number of transferrin receptors on the cell surface.[14] As ruthenium mimics iron, it is more likely to be delivered to malignant cells, resulting in higher selectivity and less toxicity towards healthy tissue.[47] In addition, the bioavailability of its various oxidation states plays a crucial role in terms of selective delivery to cancerous tissues. Although both ruthenium(II) and ruthenium(III) species are accessible under physiological conditions, ruthenium in higher oxidation state tends to be more inert whilst the reduced state appears to be more active.[45] Furthermore, compared to healthy tissue, tumour cells exhibit higher levels of glutathione, lower pH, and lower oxygen concentration due to the altered metabolism, thus creating a highly reducing environment.[48] As a result, the formerly inert ruthenium(III) species can readily be reduced to the more bioactive ruthenium(II), enhancing therapeutic efficacy.[14,45] Conversely, when ruthenium(II) leaves the cancer cells, it can be oxidized back to the inert ruthenium(III) form, thereby minimizing severe side effects.[45] Thus the difference in redox potential of both species can be used to precisely target tumour cells without affecting non-malignant tissues.

Similar to platinum, the antitumor action of ruthenium is based also on its binding to DNA.[47] However, the mode of action of ruthenium binding to DNA differs not only in comparison to platinum-based drugs, it differs in between the different species of anticancer organometallic ruthenium complexes as well.[47] Further deepening the process of (η^6-arene)ruthenium(II)

complexes binding to DNA, the binding mode of other ruthenium complexes can be found in corresponding literature.[15,47,49] Of course other targets, like serum proteins might also be very important for ruthenium compounds.[14]

1.3.2.1 (η^6-Arene)ruthenium(II) complexes

Specific family of ruthenium anticancer agents are (η^6-arene)ruthenium(II) complexes.[47] Organometallic arene complexes are compounds in which an aromatic moiety is bound to the central ion due to π-bonding, occupying formally three coordination sites.[50] Since arene ligands are strongly bound to the central ion, the ruthenium(II) ion is stabilised, preventing immediate oxidation to ruthenium(III).[50] Additionally, most of the complexes provide aqueous solubility and may hydrolyse forming the more active aqua complexes.[50] However, the (η^6-arene)ruthenium(II) moiety can be also inert towards hydrolysis, providing high stability in aqueous solution.[50] Considering the fact that these compounds are likely to bind to DNA in different ways than ruthenium(III) complexes,[49] the interest of research on this specific type of complexes for anticancer treatment hence is clarified.

The bioactivity of (η^6-arene)ruthenium(II) complexes is based on a different mode of action towards DNA compared to common platinum based drugs. Providing the possibility of interacting with DNA by intercalation, unlike cisplatin, these complexes are not cross-linking with DNA, which is creating chances to overcome disadvantages of current chemotherapeutics. Further, these compounds can be divided into two groups of arene complexes, one with polycyclic arene (e.g., biphenyl (bip), dihydroanthracene (dha), tetrahydroanthracen (tha)), the other with monocyclic ligands (e.g., benzene (ben), mesitylene (mes), *p*-cymene (*p*-cym)). Evaluating DNA interactions of various $[(\eta^6\text{-arene})Ru(en)Cl]^+$ (en = ethylenediamine) complexes, *Novakova et al.* suggest that complexes containing polycyclic rings are binding to DNA via an intercalation process, whereas complexes with monocyclic ring ligands are forming a monofunctional adduct.[50] Providing an extended π-electron system, polycyclic ligands such as tha have the ability to intercalate between base pairs of DNA double helix due to hydrophobic π-π stacking interactions, leading to a more than three times faster reaction in comparison to those of ruthenium(II) complexes bearing monocyclic ligands.[50] Since the π-electron system of monocyclic ligands like *p*-cym is fully involved into binding to the central ion, intercalation is not possible resulting in a different mode of action towards DNA.[50] (η^6-Arene)ruthenium(II) complexes with monocyclic ligands form a monofunctional adduct of the complex with DNA, resulting in an thermodynamically destabilized DNA.[50] Although interacting with DNA is happening in different modes, both groups of (η^6-arene)ruthenium(II) complexes were shown to preferentially bind to guanine residues in DNA.[50] Further evaluation if the conformation of DNA modified by monofunctional (η^6-

arene)ruthenium(II) complexes has effect on cytotoxicity, *Novakova et al.* discovered that (η^6-tha)ruthenium(II) is approximately 20 times more active than the comparable (η^6-*p*-cym)ruthenium(II) complex.[51] However, the distortion and destabilization in DNA induced due to binding of (η^6-*p*-cym)ruthenium(II) is higher than that of the related polycyclic complex.[51] Further it was found that the (η^6-*p*-cym)ruthenium(II) complex is removed by repair mechanisms more effectively from DNA than the corresponding tha complex.[51] Nevertheless it was shown that (η^6-arene)ruthenium(II) complexes are removed by different repair mechanisms than cisplatin, underlining a different mode of action of these compounds in comparison to platinum based drugs.[51] Considering all previous findings it can be clearly stated that (η^6-arene)ruthenium(II) complexes were proven to be a promising class of anticancer agents, thus requiring further research.

1.3.2.2 Ruthenium(II)-pyrithione

As previously described, the anticancer activity of ruthenium compounds, especially (η^6-arene)ruthenium(II) complexes was reported in several studies.[15,16,47,51] Additionally the ability of pyrithione to function as ionophore was suggested in literature.[35,42] However, their combination is likely to improve the biomedical properties of both species. For instance, *Kljun et al.* reported the synthesis of novel cym-bearing ruthenium(II) complexes with pyrithione and its oxygen analogue 2-hydroxypyridine-*N*-oxide.[52] Evaluating the activity of these compounds towards three enzymes of the aldo-keto reductase subfamily 1C (AKR1C), it was found that both ruthenium(II) complexes are able to inhibit all three recombinant human AKR1C enzymes[52] which are related to development of hormone dependent cancers[53] as well as resistance towards common anticancer drugs.[54] Especially the complex [(η^6-p-cym)Ru(pyrithione)Cl] (**1**, Figure 3(A)) has a high selectivity towards AKR1C1 and AKR1C3 enzymes inhibiting them irreversibly.[52] Additionally **1** was shown to have cytotoxic effects towards breast cancer cell line MCF-7, assuming an association between AKR1C enzyme inhibition and anticancer activity.[52] The further research of this promising compound revealed inhibitory effects on glutathione-*S*-transferases (GSTs) without showing cytotoxicity towards healthy cells, indicating that **1** is able to inhibit various enzymes playing a crucial role in the development of breast cancer.[55] Modifying this complex by attaching a methyl group at positions three to six of the pyrithione ligand, *Kladnik et al.* discovered enhanced *in vitro* activity of [(η^6-*p*-cym)Ru(3-Me-pyrithione)Cl] (3-Me-pyrithione = 1-hydroxido-3-methylpyridine-2(1*H*)-thionato) (Figure 3(B)) towards several cancer cell lines whilst showing the lowest toxicity towards normal cells among the evaluated compounds.[56] Due to the development of higher level of reactive oxygen species (ROS) as well as G1 cell cycle arrest, a multi-target mode of action of the parental and modified ruthenium(II)-pyrithione complex can be suggested.[56] As a

result of the previously described unique properties against malignant cells, **1** and its derivatives have been shown to be highly promising anticancer agents.[51,57] Therefore, further research and studies on these compounds and possible applications should be conducted.

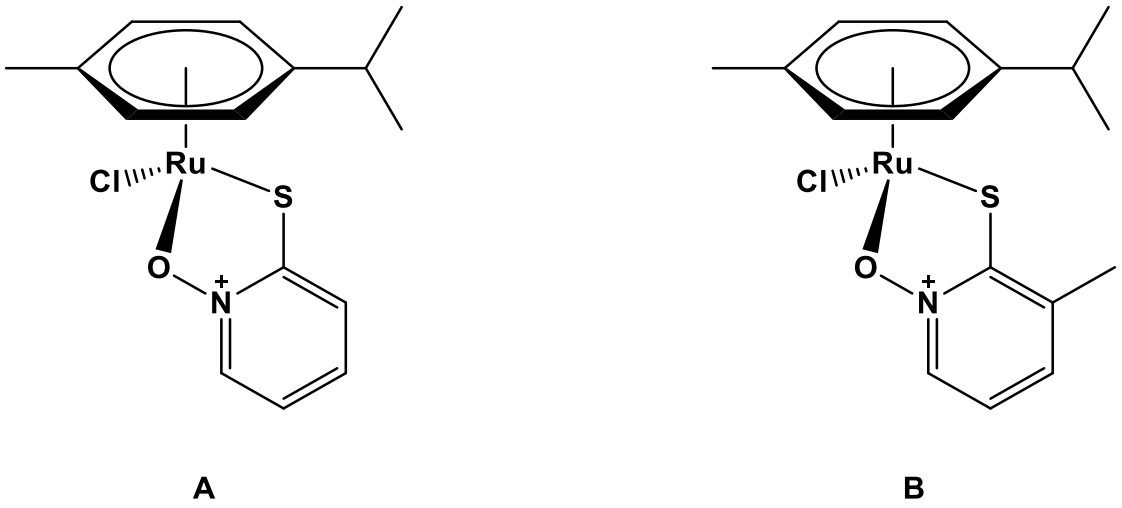

*Figure 3: Structures of **1** (A) and its 3-methyl derivative (B)*

1.4 MSNs as drug carriers for organoruthenium(II) complexes

Despite the promising bioactive properties of organoruthenium(II) compounds, their use as metal drugs in cancer therapy might be limited due to their susceptibility to healthy tissue, low solubility in aqueous solutions and not fully defined mode of action on cancer cells.[14,47] The use of MSNs as carrier systems for ruthenium(II) complexes therefore appears to be a great opportunity to overcome these drawbacks by enhancing the solubility and stability in aqueous solutions as well as providing high selectivity towards malignant cells due to the affinity of MSNs to accumulate in tumour sites.[14,31,58] Recent studies focusing on the immobilization of organoruthenium(II) complexes on functionalized MSNs as drug carriers reveal enhanced cytotoxic effects as well as significantly extended cellular uptake in cancer cells.[58,59] For instance, *He et al.* studied the effect of monodisperse MSNs as carriers for ruthenium polypyridyl complexes towards cellular uptake, bioactivity and drug release in cancer cells *in vitro*.[58] Synthesizing ruthenium-polypyridyl loaded MSNs by surface functionalization with arginine-glycine-aspartic acid peptide sequence (RGD-sequence), it was shown that the loaded MSNs effectively enhance the cellular uptake of the bioactive ruthenium(II) species *via* receptor-mediated endocytosis thereby improving the selectivity between cancer and normal cells.[58] Afterwards, releasing free ruthenium species into the cytoplasm and consequently leading to ROS overproduction. The MSNs loaded with ruthenium(II) complexes promote apoptosis leading to inhibition of tumour growth.[58] *Mladenovic et al*. were focused on the

release of ruthenium metallotherapeutics from MSNs depending on pH-value. Functionalizing the nanocarriers with two different types of hydrazine ligands and further binding the corresponding (η^6-p-cym)ruthenium(II) species into the MSNs, it was shown for these materials that the release of reactive ruthenium(II) complexes is enhanced in weakly acidic conditions.[59] The decreased pH-value present in tumour sides provides perfect conditions to hydrolyse the pH-responsive hydrazone bond present in ruthenium(II) complexes, hence leading to the enhanced release of active species and further improved selectivity and cytotoxicity *in vitro* in B16F1 melanoma cell lines.[59] These results underline the potential use of functionalized MSNs as a drug delivery system. Providing a polar Si-OH surface, it is moreover likely that drug loading of the MSNs could be improved by the addition of polar functional groups on the organometallic complexes. However, the immobilization of ruthenium(II) chemotherapeutics on silica nanocarriers with and without prior functionalization and their *in vitro* potential effects need to be further investigated.

1.5 Aim of the work

(η^6-Arene)ruthenium(II) complexes, for example [(η^6-*p*-cym)Ru(pyrithione)Cl] (**1**) and its derivatives, have been shown to provide cytotoxic effects on malignant cells of various cancer cell lines.[52,56] However, their application as anticancer drugs might be limited due to the not yet fully characterised modes of action, the early stage of research on these compounds as well as the common problems of chemotherapeutics such as low solubility and cytotoxicity towards normal cells. The use of nanostructured mesoporous silica as a delivery system is likely to overcome certain disadvantages in terms of selectivity and bioavailability, leading to lower dosages applied. Recent studies have shown that MSNs loaded with organoruthenium(II) complexes show promising anticancer results, even compared to cisplatin. Modification of bioactive ruthenium(II) complexes such as **1** was shown to improve their bioactivity. Synthesis of novel ruthenium(II) pyrithione derivatives by introduction of functional groups at the pyrithione ligand hence could improve either their anticancer properties or the adsorption into MSNs for usage in delivery systems.

The aim of this work will be the synthesis of **1** and its derivatives, bearing polar functional groups (carboxylic or ester) thus combining cytotoxic moiety ((η^6-arene)ruthenium(II) moiety) alongside to ionophore with anti-inflammatory properties (pyrithione and derivatives). Synthesized compounds will be characterised using common methods such as ^{1}H and ^{13}C NMR spectroscopy and purity will be examined by EA. Due to promising drug delivery properties of MSNs especially for tumour targeting, synthesized ruthenium(II) complexes will be immobilized into two mesoporous nanostructured silica particles MCM-41 and SBA-15. The carriers without and with loaded ruthenium(II) complexes will be characterized using BET-analysis, SEM, DLS and EDX.

2 Results and discussion

2.1 Synthesis of pyrithione derivatives

Pyrithione was chosen as ligand due to its ability to enhance intracellular metal ion concentration as well as providing anti-inflammatory properties as described previously. Derivatives of pyrithione, especially with additional carboxylic acid and ester group bound to the 3rd position aromatic carbon atom, presumably increase the bioavailability as well as the adsorption of the corresponding organoruthenium(II) complexes in MSNs. Whilst the unmodified pyrithione ligand 1-hydroxy-2(1*H*)-pyridinethione (**HL1**) is commercially available, derivative 1-hydroxy-2-thioxo-1,2-dihydropyridine-3-carboxylic acid (**H_2L2**) bearing a carboxylate group at position 3 (Figure 4) is prepared by oxidation and subsequent thiolation of methyl 2-chloronicotinate (M2CN). Corresponding ethyl ester ethyl 1-hydroxy-2-thioxo-1,2-dihydropyridine-3-carboxylate (**HL3**) is prepared by esterification of **H_2L2**.

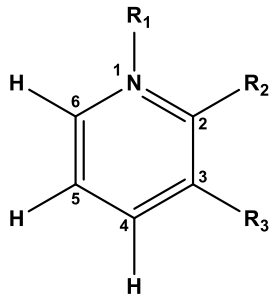

R_1: /, -O
R_2: -Cl, -SH
R_3: -COOMe, -COOH, -COOEt

Figure 4: Numeration of carbon atoms in pyridine and its derivatives

2.1.1 Synthesis and characterization of H_2L2

2.1.1.1 Oxidation reaction

For the synthesis of **H_2L2**, first methyl 2-chloronicotinate (M2CN) is oxidized using two molar equivalents of urea-hydrogenperoxide (UHP) in the presence of trifluoroacetic anhydride (TFAA) to form the intermediate 2-chloro-3-(methoxycarbonyl)-pyridine-*N*-oxide (**I1**). The mixture of UHP and TFAA is resulting in the highly oxidative peroxitrifluoroacetic acid, further interacting with M2CN to form **I1**.[60] The reactants are dissolved in dichloromethane (DCM) and stirred at room temperature for at least 4 h (Scheme 1). After the reaction the solution is quenched with 2 M HCl, hydrolysing TFAA. Subsequently the organic phase is extracted twice using saturated Na_2CO_3 solution, removing excess of acid and UHP. Finally, the oxidized

product is obtained by evaporating the solvent after drying over Na_2SO_4, yielding a yellowish crystalline solid.

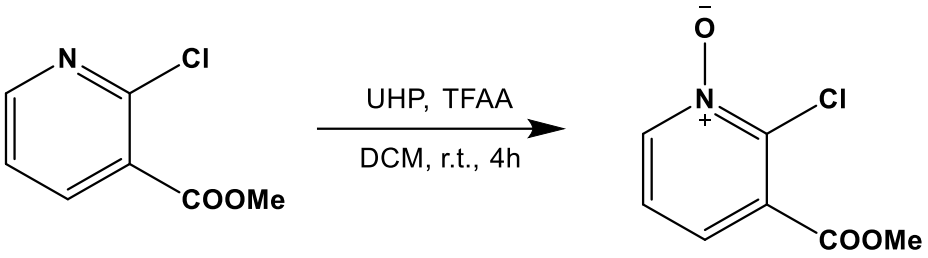

Scheme 1: Oxidation of methyl-2-chloronicotinate

To verify if the oxidation reaction is leading to the desired product, a comparison of ^{1}H NMR spectra of M2CN and **I1** is used as shown in Figure 5. All hydrogen resonances in M2CN (lower spectra) can be found as expected. Namely, in the ^{1}H NMR spectrum of **I1** two doublet of doublet shifts are assigned to resonances for the aromatic hydrogen atoms at 8.49 and 8.14 ppm. A triplet shift at 7.31 ppm belonging to aromatic hydrogen at position five can be detected as well as an intense singlet derived from the CH_3 group at 3.93 ppm (Figure 4). Due to the introduction of oxygen bound to the N atom of the pyridine ring, the chemical environment of positions two and six (Figure 4) should be affected the most. Inducing an +M-effect, the introduction of oxygen atom is leading to a higher shielding of atoms bound to the aromatic ring, further resulting in an upshift of correlating resonances. A significant difference after oxidation (8.14→7.66 ppm; red box in Figure 5), can be assigned to C^6*H* located in close environment of NO group. The chemical shift at 8.49 ppm is assigned to hydrogen atom from C^4*H*. These results point out the successful oxidation reaction, leading to the desired product **I1**. This is further confirmed comparing the spectral results of **I1** to literature.[61]

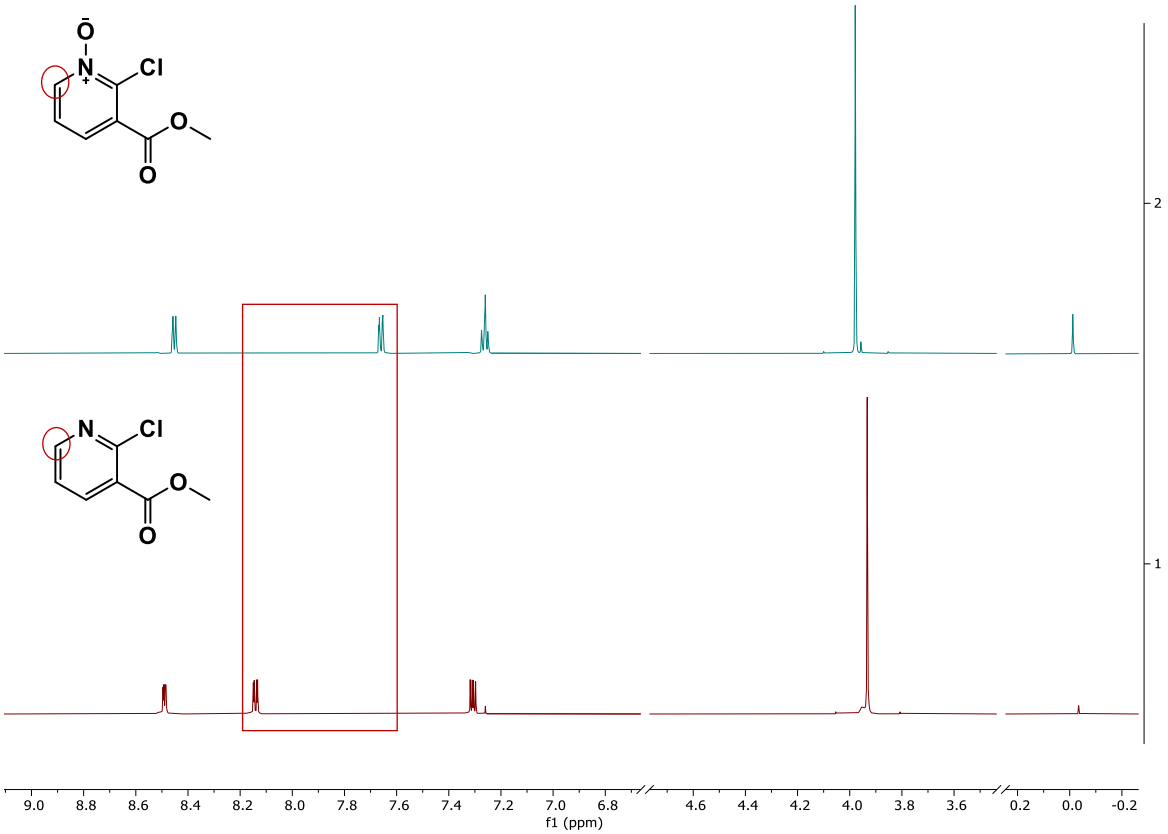

*Figure 5: ^{1}H NMR spectrum of M2CN (lower) and **I1** (upper); in $CDCl_3$ (600 MHz)*

2.1.1.2 Thiolation reaction

To further introduce sulphur to the formed *N*-oxide product, a three-step reaction of thiolation is used (Scheme 2). First of all, thiourea as sulphur source is stirred with the *N*-Oxide intermediate **I1** in ethanol under reflux thereby inducing a nucleophilic attack of thiourea substituting the chloride leaving group via S_N2-mechanism. The formatted thioether is precipitating as yellow solid. In the second step, after filtration, the intermediate product is dissolved in aqueous solution of 0.5 eq. of K_2CO_3, further adding three eq. of dissolved NaOH and stirring at higher temperature. The aqueous alkaline solution thus is hydrolysing the intermediate thioether, forming urea, methanol and the corresponding thiolate and carboxylate, respectively. In the last step concentrated HCl is added until pH 1, protonating the ligand-anion. Formed acid (**H_2L2**) precipitated as bright yellow solid.

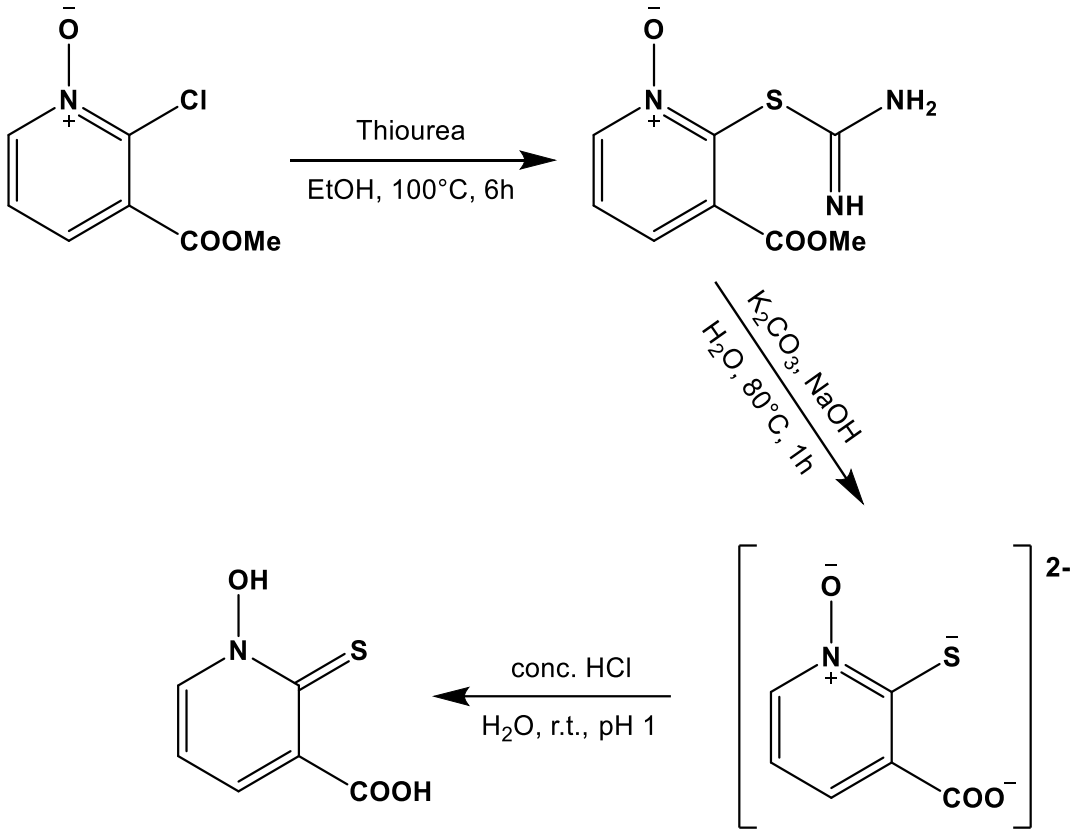

*Scheme 2: Thiolation reaction for synthesis of **H_2L2***

The obtained thiolation product **H_2L2** was analysed using ^{1}H and ^{13}C NMR spectroscopy (Figure 6). The two broad resonances recorded at 14.7 ppm and 12.7 ppm can be presumed to correspond to the carboxylic acid and hydroxy group introduced by thiolation due to the tendency of hydrogen atoms bound to polar groups to interact with solvent[62], whereas it cannot be clearly defined which chemical shift belongs to which proton. As presented in Figure 6, the aromatic hydrogen atoms present in **I1** can be detected in **H_2L2** as well, showing significant shifts for the resonances of hydrogen atoms at C^5H and C^6H (7.51→7.04 ppm; 7.72→8.12 ppm; red box in Figure 6). Shifts can be explained due to inductive effects deriving from introduction of sulphur and substitution of methoxy group. Comparing spectra of **I1** and **H_2L2**, the resonances for the methyl ester group present in **I1** (green box in Figure 6) cannot be found in **H_2L2**, emphasising the hydrolysis of methyl ester group to form the carboxylic acid (green box in Figure 6). Consequently, the recorded product can be presumed as Ligand **H_2L2**. This assumption is verified comparing the results with ^{1}H NMR spectra presented in the literature.[61]

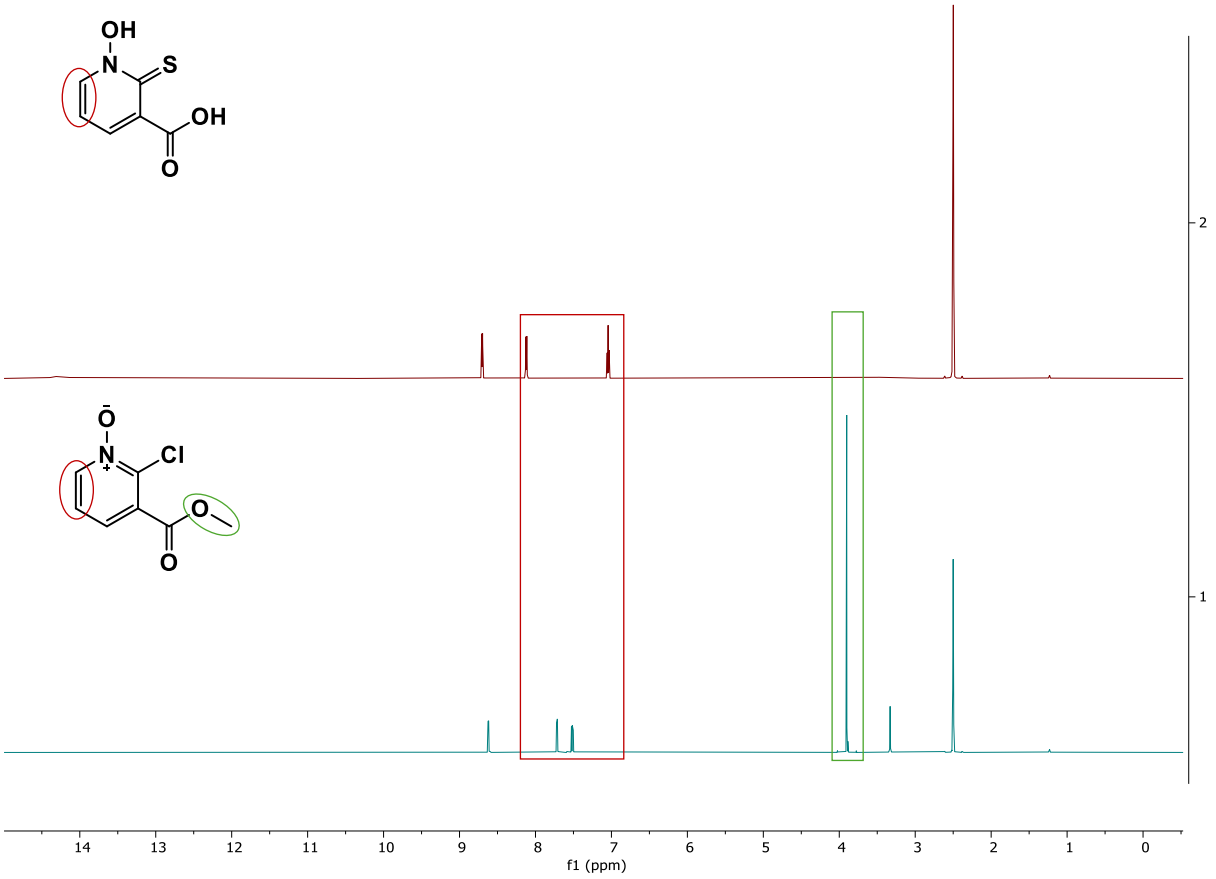

*Figure 6: ^{1}H NMR spectra of **I1** (lower) and **H_2L2** (upper); in DMSO-d_6 (600 MHz)*

2.1.2 Synthesis and characterization of HL3

For the introduction of an ester group at position three, the previously described acid **H_2L2** was used as starting compound. Within the trial of two different ways of esterification, a synthesis route using $SOCl_2$ described in literature[63] showed more promising results than acid-catalyzed esterification route using concentrated sulphuric acid.

Firstly, five molar eq. of $SOCl_2$ and **H_2L2** are dissolved in ethanol while stirring on ice. In this process the intermediate carboxylic acid chloride is formed due to *S_N2* substitution, releasing SO_2 and HCl as side products. Subsequently heated up to boil under reflux, the nucleophile ethanol is interacting with the intermediate acid chloride in an S_N2-mechanism, thus forming the ethyl ester Ligand **HL3** under production of HCl. The reaction is stopped after verification of product formed using thin layer chromatography (TLC). After evaporation of the solvent, the product was cleaned by column chromatography using 2% MeOH/DCM as mobile phase. The solid green-brown product was obtained by evaporation of the mobile phase. Starting compound **H_2L2** is not moving on the column.

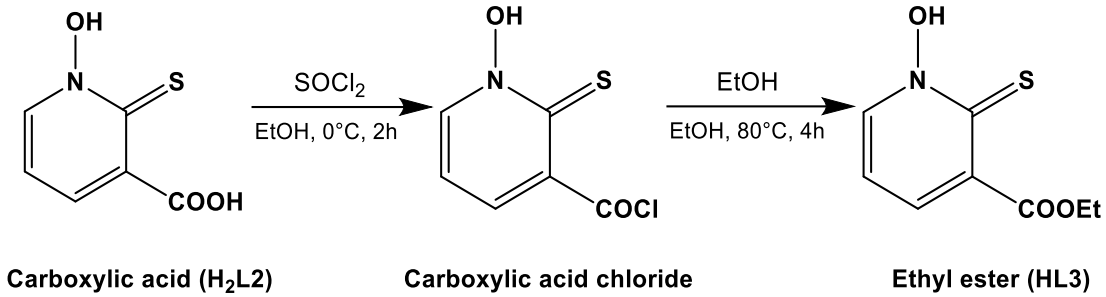

*Scheme 3: Synthesis of ester **HL3** from acid **H₂L2***

As an example of purification attempts the ^{1}H NMR spectra of **HL3** before are shown in Figures A6–A8 in the appendix. It can be clearly seen that major impurities mainly from unreacted starting compound **H₂L2** could be removed using column chromatography. Comparing the ^{1}H NMR spectra of **H₂L2** and **HL3**, chemical shifts of all aromatic hydrogen resonances can be detected showing a significant difference for hydrogen atom C^{6}*H* (8.12→7.73 ppm; Figure 7 marked red). Due to the +I-effect of the introduced ethoxy group this seems plausible. Furthermore, two new resonances can be detected in the alkyl region, a quartet at 4.28 ppm as well as a triplet at 1.29 ppm assigned to CH_3CH_2 moiety (marked green in Figure 7). Furthermore, resonance at 12.59 ppm (C^{7}OO*H*; marked blue) present in **H₂L2** due to esterification (→ **HL3**) could not be detected in ^{1}H NMR spectrum of **HL3** (Figure A4 and Figure A10). These results confirm successful esterification reaction to form the desired ethyl ester ligand **HL3**.

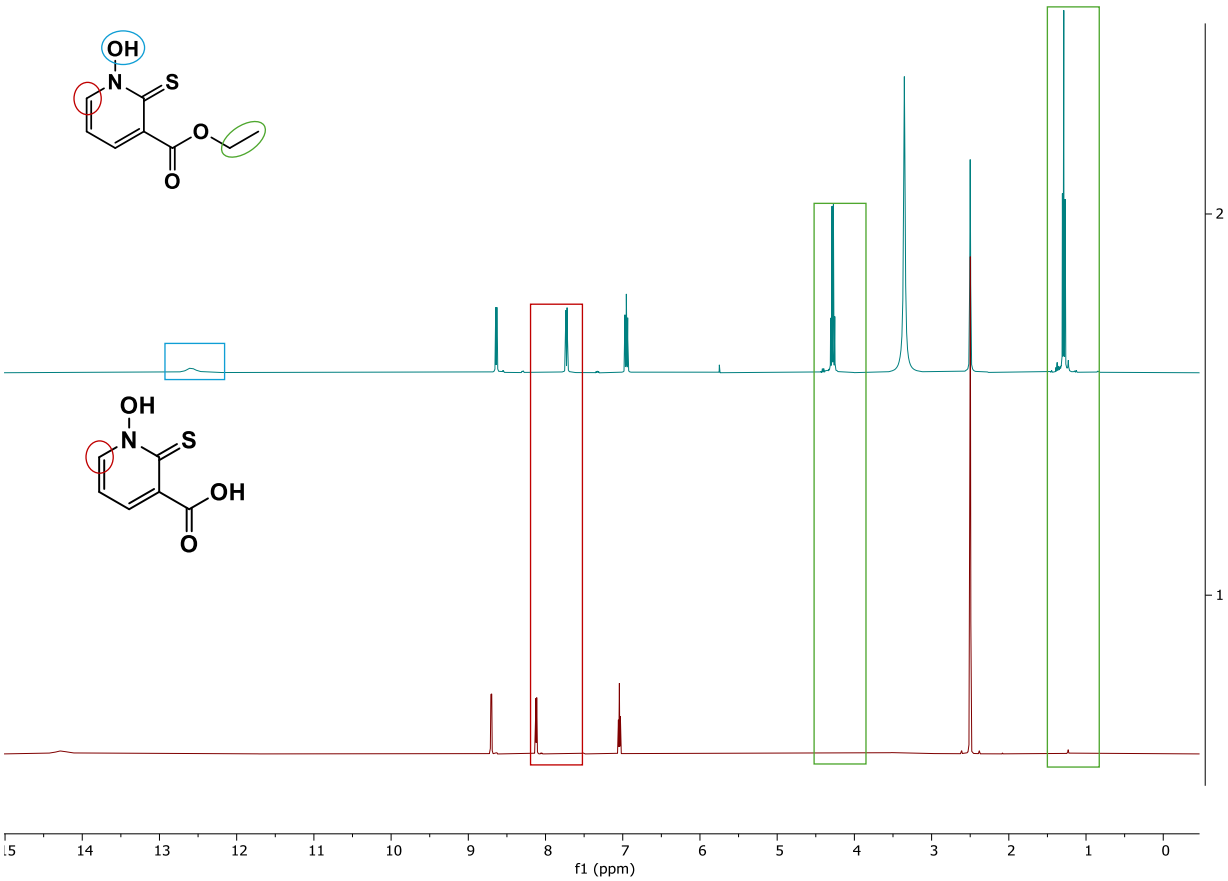

*Figure 7: ^{1}H NMR spectra of **H_2L2** (lower) and **HL3** (upper); in DMSO-d_6 (400 MHz)*

2.2 Synthesis and characterization of [(*p*-cym)Ru(L)Cl] (L$^-$ = L1$^-$, HL2$^-$, L3$^-$) complexes

Prepared ligands **HL1–HL3** are further used for the synthesis of ruthenium(II)-pyrithione complex and its derivatives with general formula [(η^6-*p*-cym)Ru(**L**)Cl] (**L$^-$** = **L1$^-$, HL2$^-$**, **L3$^-$**). Synthesis route similar to previously reported literature is used.[52,61] For this purpose dichlorido(*p*-cym)ruthenium(II) dimer, [{Ru(*p*-cymene)Cl_2}$_2$] was reacted with two molar eq. of **HL1–HL3** dissolved in DCM. Subsequently NaOMe was added and the solution stirred at room temperature. The reaction is shown in Scheme 4. After reaction was completed, red solution was filtered through a celite column using DCM as mobile phase, purifying product from NaCl as well as unreacted [{Ru(*p*-cymene)Cl_2}$_2$]. Depending on the used ligand, the product can be obtained as bright (**2**) or dark-red (**1, 3**) solid. The products were characterized by ^{1}H and ^{13}C NMR spectroscopy and the purity was confirmed by elemental analysis.

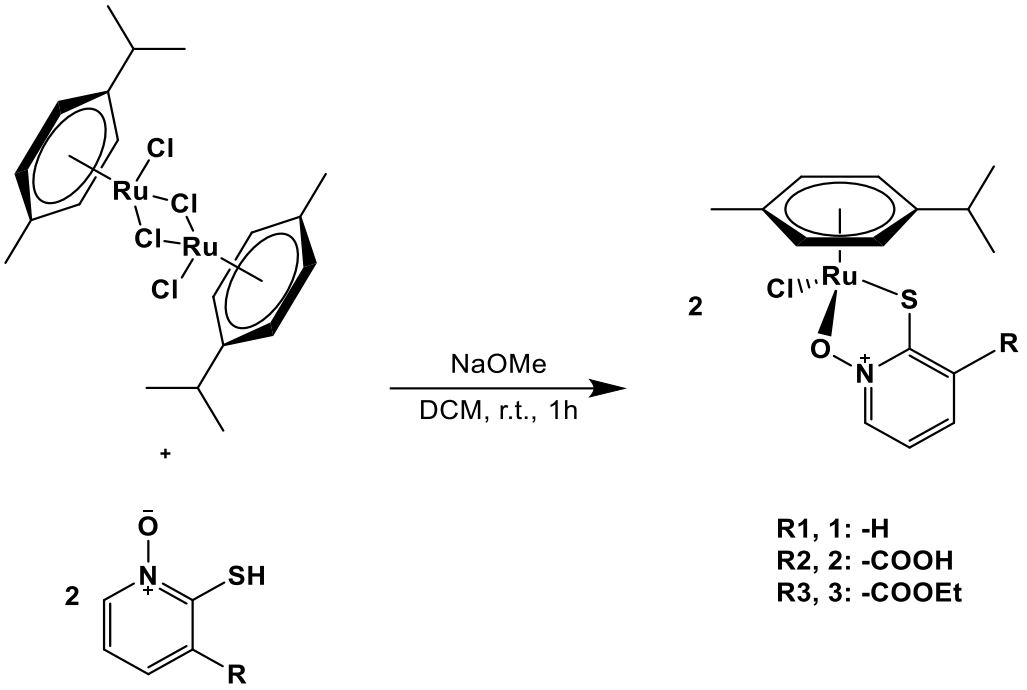

*Scheme 4: Synthesis of [(η⁶-p-cym)Ru(**L**)Cl] (**L**⁻ = **L1**⁻, **HL2**⁻, **L3**⁻) complexes*

2.2.1 [(η⁶-*p*-cym)Ru(L1)Cl] (1)

The complex [(η^6-*p*-cym)Ru(**L1**)Cl] (**1**) previously reported by *Kljun et al.* is synthesized as described above using the commercially available pyrithione (**HL1**).[52] The product was characterized using ^{1}H and ^{13}C NMR spectroscopy as well as elemental analysis. The characteristic chemical shifts of **HL1** can be found in the spectra along with the resonances of *p*-cym present in the complex. Direct comparison of reported spectra for **HL1** and **1** is not possible due to the low solubility of **HL1** in $CDCl_3$. Nevertheless, the ^{1}H NMR spectrum of **1** shows the four characteristic resonances of aromatic hydrogen atoms from **HL1** (marked red in Figure 8), as well as the aromatic proton resonances corresponding to the *p*-cym moiety (marked yellow). Methyl and isopropyl groups from *p*-cym are found at expected chemical shifts (marked green). To enable the coordination to ruthenium(II), **HL1** had to be deprotonated, leading to removal of the O*H* proton present in **HL1** (Figure A1), which hence cannot be detected in **1**. In comparison to literature all proton resonances are found at expected positions in ^{1}H NMR spectrum.

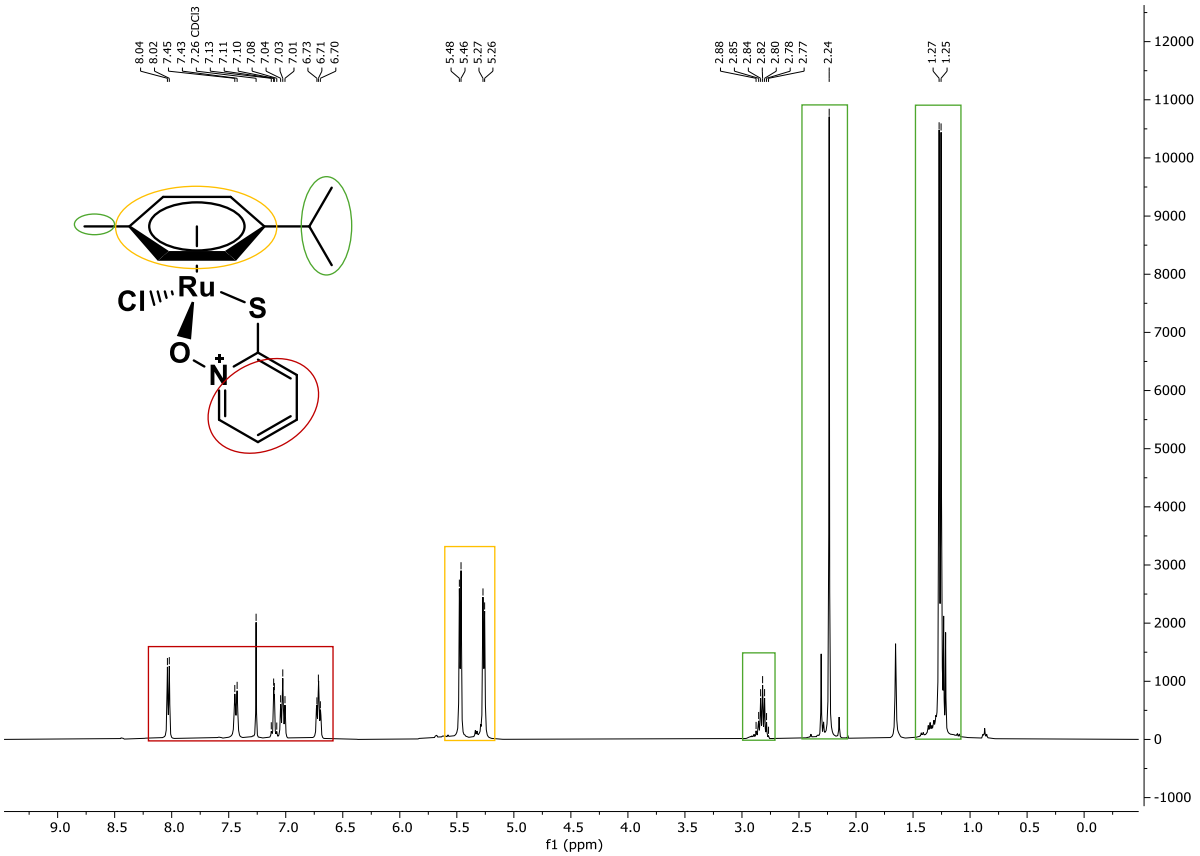

*Figure 8: ^{1}H NMR spectrum of **1**; in $CDCl_3$ (600 MHz)*

2.2.2 [(η^6-*p*-cym)Ru(HL2)Cl] (2)

Derivative complex (η^6-p-cym)Ru(**HL2**)Cl] (**2**) is synthesized using the procedure described previously and further characterized by ^{1}H and ^{13}C NMR spectroscopy as well as elemental analysis. Comparing the ^{1}H NMR spectra of **H_2L2** and **2** (Figure 9), characteristic hydrogen resonances of ligand moiety can be found, shifting significantly upfield when coordinating to the complex (marked red in Figure 9). However, coordination of **H_2L2** to the metal center should result in deshielding of ligand protons, which cannot be observed. Moreover, chemical shift belonging to COO*H* proton cannot be detected in **2** as well (marked blue). Nevertheless, ^{1}H NMR spectrum recorded for **2** can be confirmed by comparison to the results reported in the literature.[61]

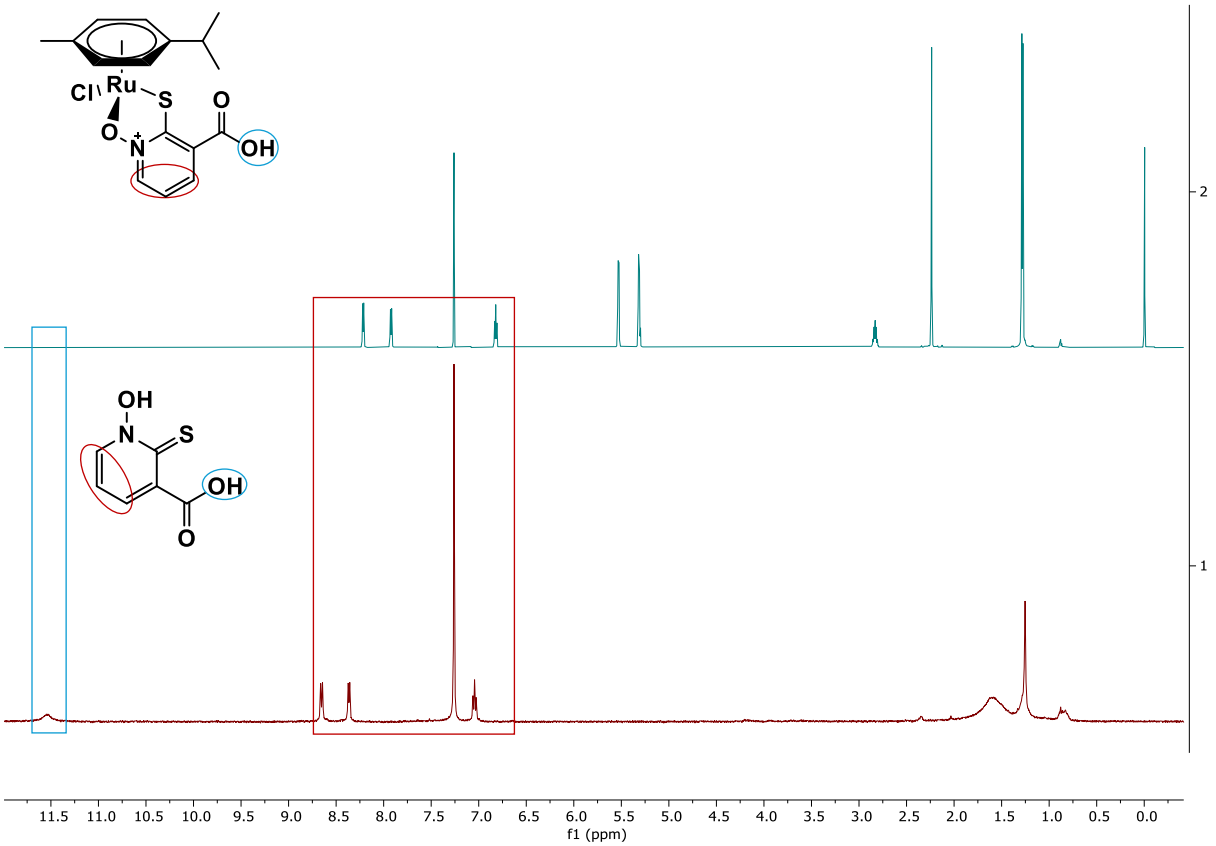

*Figure 9: ^{1}H NMR spectra of **L2** (lower) and **2** (upper); in $CDCl_3$ (400 MHz)*

Due to the unique properties of **H_2L2** containing three neighbouring functional groups that provide free electron pairs, theoretically coordination to ruthenium(II) is not only possible via (*N*)*O* and *S* (Figure 10, A), but also through *S* and (CO)O atoms (Figure 10, B) is possible as well (Figure 10). Additionally, more complex products (e.g., dimers) could also form theoretically. Comparison of ^{13}C NMR spectra of **H_2L2** and **2** could provide information about present binding mode.

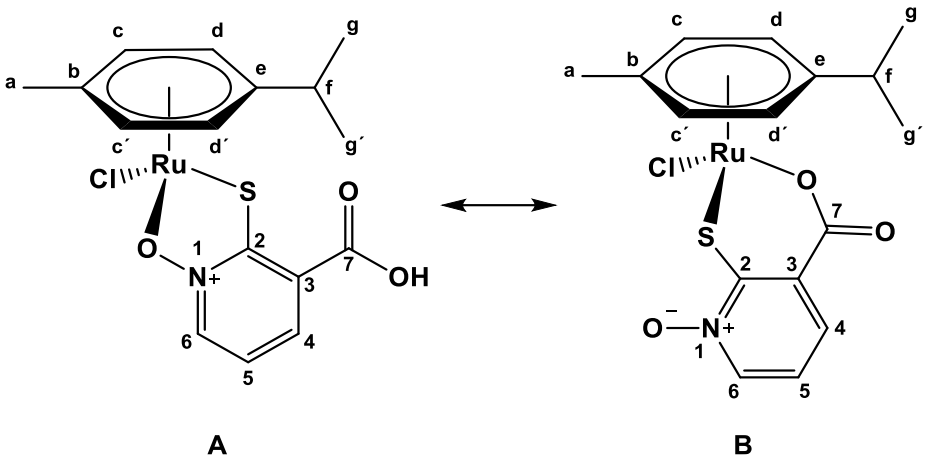

*Figure 10: Possible coordination modes of **HL2⁻** in **2** through: (N)O,S- (**A**) and S,(CO)O (**B**) donor atoms*

Relevant part of ^{13}C NMR spectra for determination of coordination mode of **HL2⁻** to ruthenium(II) (**2**) of **H_2L2** and **2** are presented in Figure 11 (spectra can be found in Figure A6 and Figure A15). The two resonances located at 165.8 and 163.7 ppm appear to belong to the C^2 (marked orange) bound to sulphur atom and the C^7 atom (marked blue) of carboxylic group, respectively. Besides it can be seen, that the C^2 and C^7 atoms upon coordination of **HL2⁻** to ruthenium(II) are downshifted (C^7: 165.8→166.5 ppm; C^2: 163.7→163.3 ppm), thereby indicating a deshielding by complex synthesis. Additionally, the C^6 atom nearest to *NO* moiety is shifted upfield (135.1→134.5 ppm, marked red), whereby a coordination via the *NO* moiety seems unlikely, implying present binding mode B. Moreover, chemical shifts corresponding to C^5 atom display most significant change upon complex reaction (113.5→116.5 ppm, marked green). This downshift can appear due to deshielding of C^5 as a result of electron movement towards C^3 and by delocalised aromatic π-electron system, thus emphasising coordination via carboxylic group. As a result of this ^{13}C NMR spectral examination, coordination mode B can be presumed to be present in **2**. However, the definitive structure of formed complex has to be further determined by X-ray structural analysis. Nevertheless, complex **2** was chosen to be used for immobilization attempts due to sufficient purity confirmed by elemental analysis.

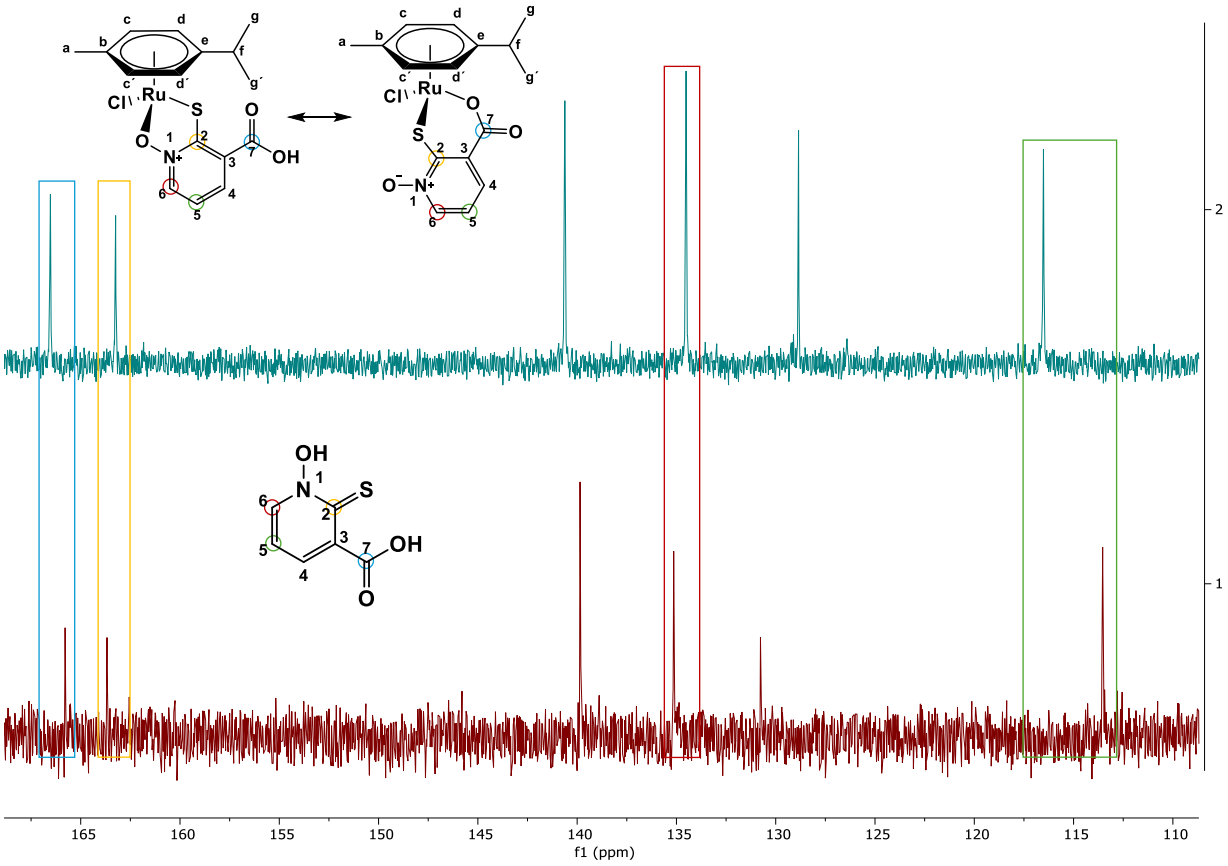

*Figure 11: Comparison of ^{13}C NMR spectra (relevant part) of **H_2L2** (lower) and **2** (upper); in $CDCl_3$ (100 MHz)*

2.2.3 [(η⁶-*p*-cym)Ru(L3)Cl] (3)

Derivative [(η^6-p-cym)Ru(**L3**)Cl] (**3**) is synthesized using procedure described previously and further characterized by ^1H and ^{13}C NMR spectroscopy as well as elemental analysis. ^1H NMR spectrum of **3** (Figure 12) revealed similar chemical shifts for pyrithione (marked red) and *p*-cym moieties (marked orange) as in previously described ruthenium(II) complexes **1** and **2** (Figure 8 and Figure A14). Broad resonance of N-O*H* present in **HL3** (Figure A10) cannot be detected. Ethyl ester ligand moiety (marked green) could be detected at 4.38 ppm (C$^8H_2$, quartet) and 1.38 ppm (C$^9H_3$, triplet) as well, thus emphasising formation of complex **3**.

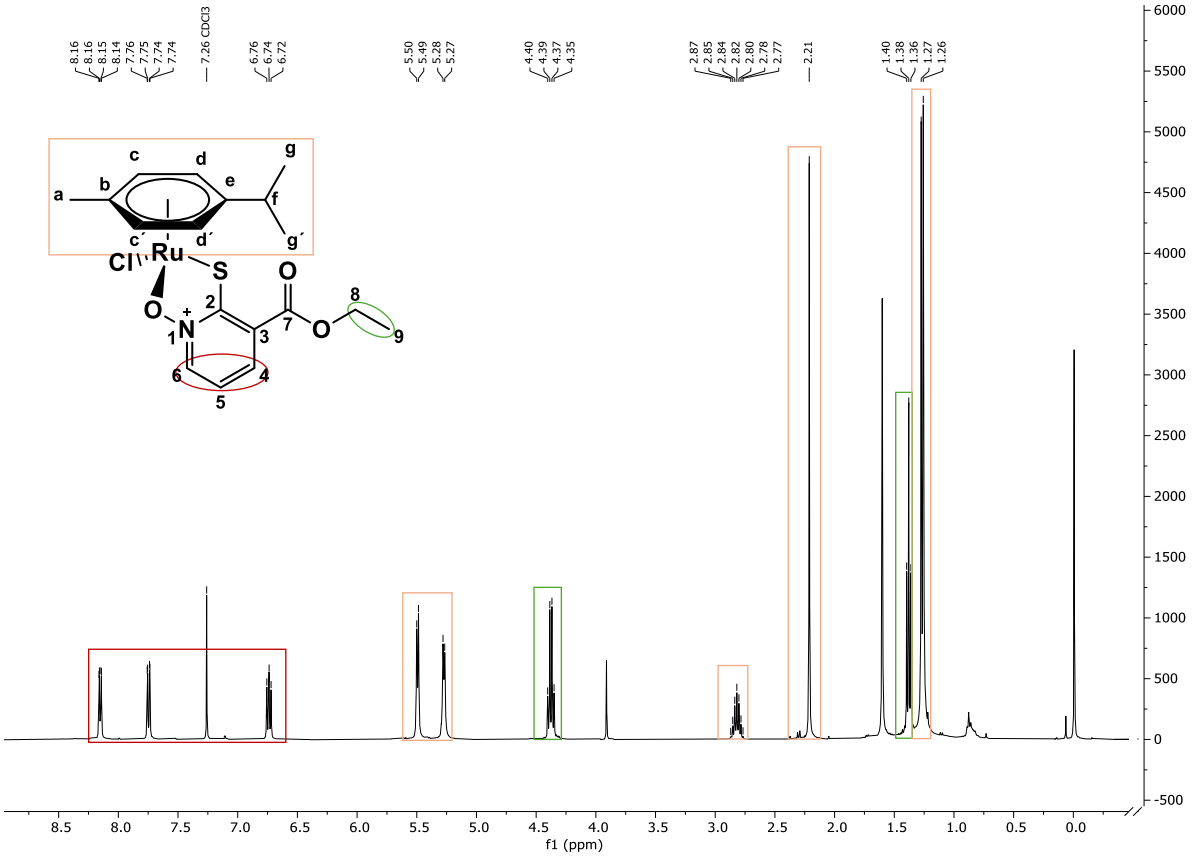

*Figure 12: ^{1}H NMR spectrum of **3**; in $CDCl_3$ (400 MHz)*

^{13}C NMR spectrum of **3** is presented in Figure 13. Most deshielded ligand carbon atoms C^{7} and C^{2} (marked blue) can be detected far downfield at 164.1 ppm and 163.5 ppm, respectively. Aromatic carbon atoms of **HL3** (marked red) as well as carbons of *p*-cym moiety (marked orange) revealed similar chemical shifts as in complexes **1** and **2** (Figure A13 and Figure A15). Resonances detected at 62.0 (C^{8}) and 14.4 ppm (C^{9}) can be assigned to ethyl ester moiety of **HL3**. Hence, formation of complex **3** is verified.

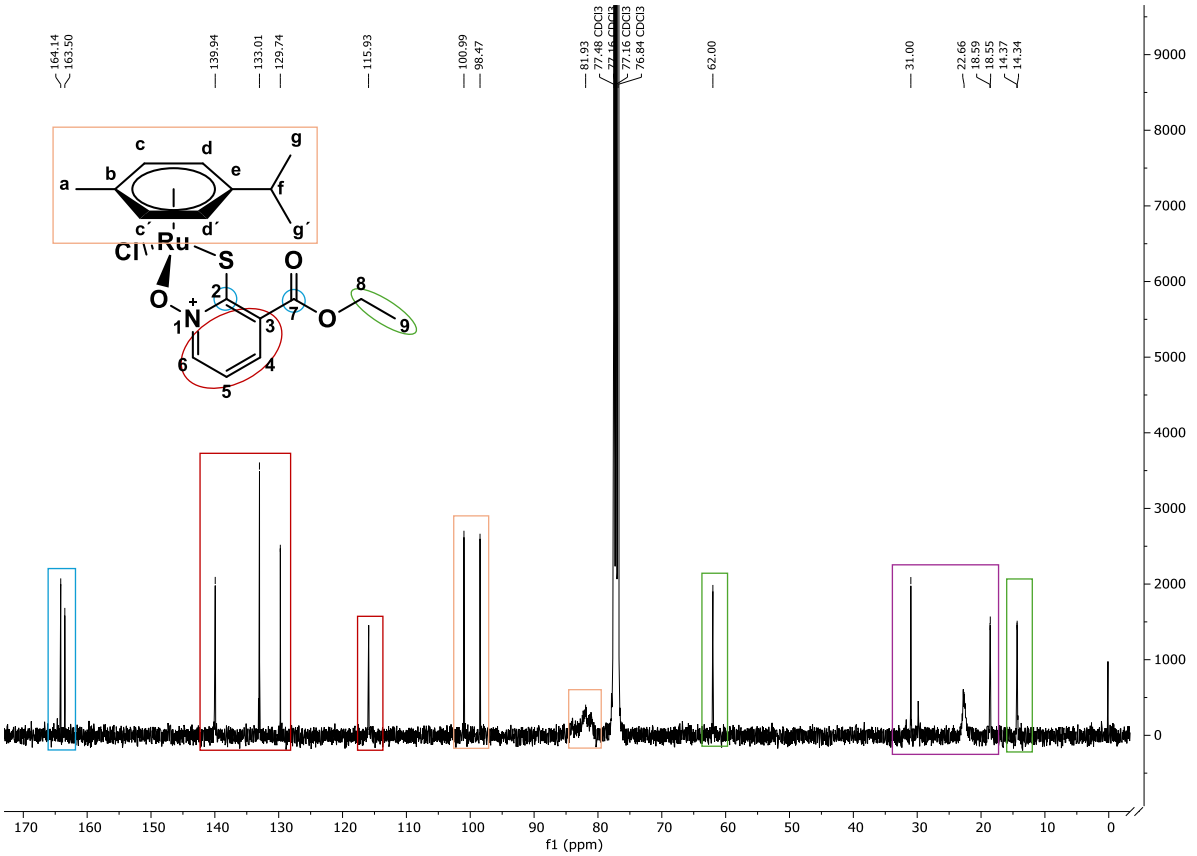

*Figure 13: ^{13}C NMR spectrum of **3**; in $CDCl_3$ (100 MHz)*

2.3 Synthesis and characterization of mesoporous nanostructured silica

In order to immobilize the prepared active compounds **1–3** into different species of mesoporous nanostructured silica, the two commonly used MSNs MCM-41 and SBA-15 were chosen as carrier system. Therefore, synthesis and characterization for both nanostructures is described further.

2.3.1 Synthesis and characterization of MCM-41

MCM-41 was synthesized with slightly changed established procedure reported by *Tao et al*.[64] The used cationic tenside CTAB is stirred in water until complete dissolution, thereby forming characteristic micelles necessary for structural direction. Furthermore, the solution is heated up to 70 – 80 °C with subsequent addition of NaOH and TEOS. In the present alkaline solution, hydrolysis of TEOS into orthosilicic acid is catalysed, thus forming silica species with negative charge. Due to electrostatic interactions the silica species coordinate to the positively charged tenside molecules thereby starting the formation of solid SiO_2 predefined by SDA-micelles.

After aging, the solid product was filtered, washed and calcinated to completely remove CTAB, yielding the solid white material. Characterization of produced MCM-41 using scanning electron microscopy (SEM) is shown in Figure 14. The majority of particles synthesized showed spherical structures with sizes varying from 880 to 930 nm. Although showing a high degree of homogeneity, produced particles appear to be at the upper border of size suitable for usage as nanocarriers, ranging between 800 – 1000 nm.[19,64] This has been confirmed using dynamic light scattering (DLS; Figure A16). *Tao et al.* MCM-41 sized between 500 – 900 nm.[64] However, the shape, homogeneity and size range of synthesized MCM-41 is sufficient for use as carrier for immobilization attempts evaluated in this work.

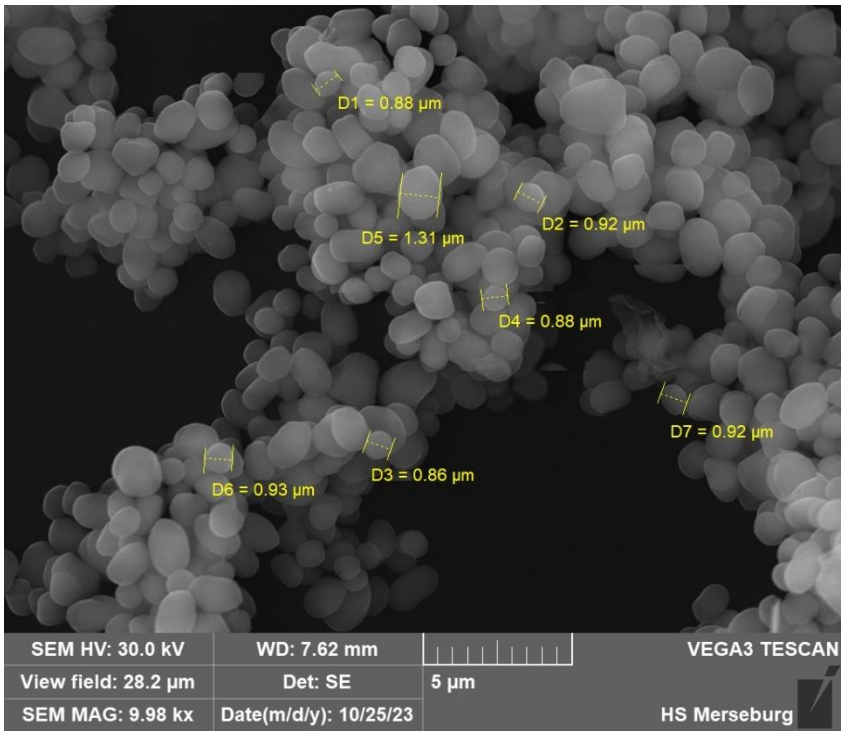

Figure 14: SEM of MCM-41

The specific surface area of produced particles was determined by nitrogen sorption analysis using the method of Brunauer-Emmett-Teller (BET-analysis). Nitrogen isotherms of adsorption (red) and desorption (blue) are shown in Figure 15. Measured adsorption and desorption isotherms can be identified as type IV(a) corresponding to mesoporous materials according to IUPAC.[65] Further a division into three sections can be made.

Within the first section occurring at low relative pressures, the isotherm is increasing nearly linear. By increasing the pressure, nitrogen molecules constantly layer on the surface of pore walls, leading to formation of a monolayer where every molecule interacts with the particle surface. This is displayed by the sharp rise at very low p/p_0 values at the beginning of section one. The higher the pressure for adsorption is rising, the more the monolayer gets filled. When all free surface spots in the pores are occupied, molecules further adsorb to the already existing monolayer, implying that multilayer adsorption begins.[65] Multilayer adsorption occurs in linear growth, displayed by the nearly linear slope at the end of section one, forming a plateau. The sudden rise of isotherm in section two can be explained due to the start of capillary condensation characteristic for mesoporous materials.[65] The Van der Waals forces present in mesopores are high enough to condense the gas below its saturation vapour pressure, followed by higher adsorption into the pores thus leading to increased slope of the isotherm. When the pores are filled completely at higher p/p_0 values adsorption happens as well on the surface of the particles. The mono- and multilayer adsorption onto the outer particle surface is displayed by section three, providing a much smaller slope of the adsorption isotherm. The way smaller slope in section three compared to section one as well as the greater extend of adsorption occurring at higher pressure is an indication that mesoporous surface of present MSN is higher than the outer surface. Due to capillary condensation forces for liquid-like gas are higher leading to a time-displaced desorption represented by characteristic hysteresis loop.[65] However, for particles with pores smaller than 4 nm, adsorption and desorption are reversible and overlapping still. Since no hysteresis loop can be detected in present BET-isotherms, adsorption and desorption takes place at equal relative pressures, indicating pore sizes below 4 nm. Nevertheless, t-plot method revealed that no micropores are present in the obtained MCM-41 and despite the small pore diameter it can be characterized as mesoporous material.

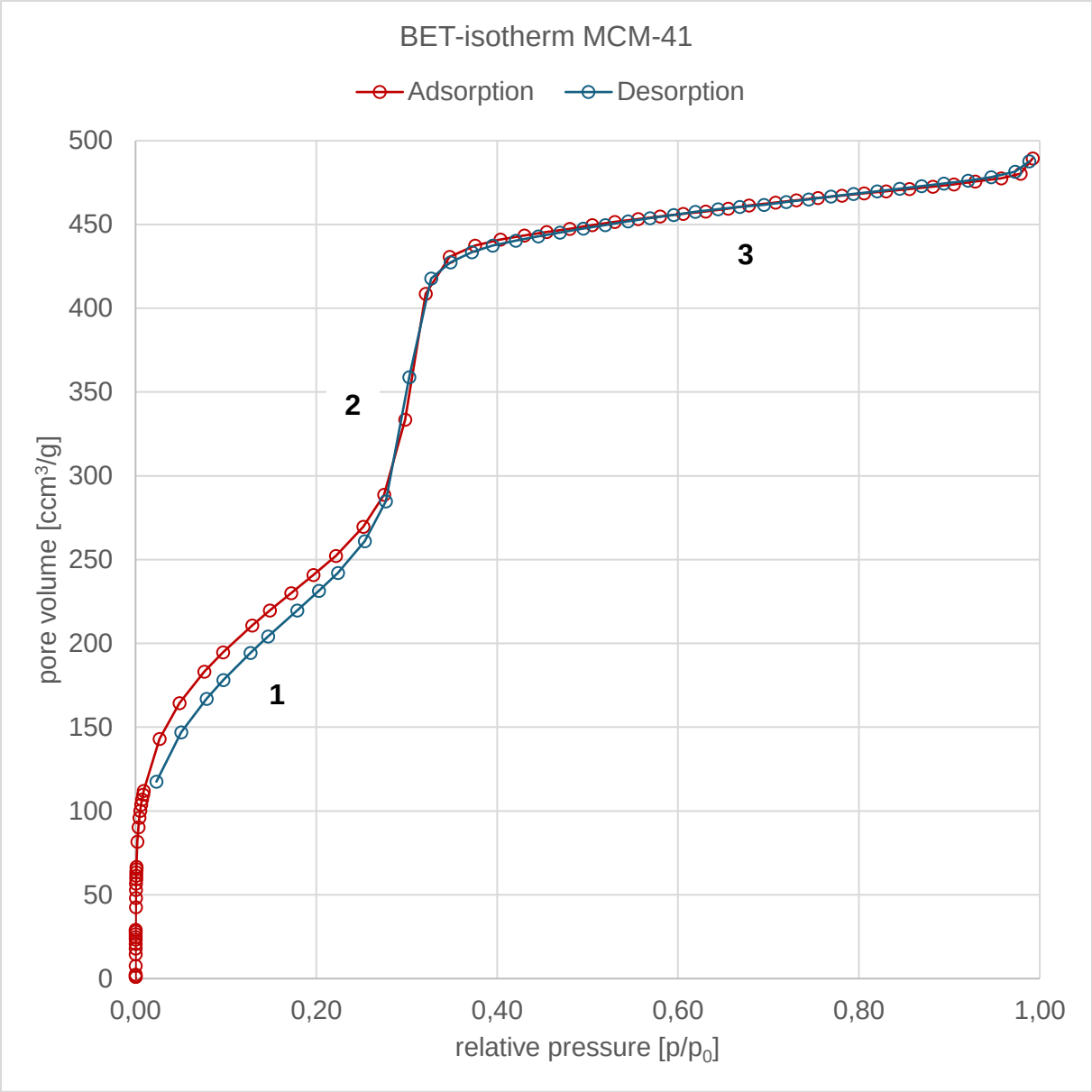

Figure 15: Adsorption and desorption isotherms of N_2 at 77 K for MCM-41

The multi-point BET analysis uses measured data between 0.05 and 0.3 p/p_0 providing a surface area of 1005.7 $m^2 \cdot g^{-1}$. The average pore diameter of 3.11 nm was calculated using Barret, Joyner and Halenda (BJH) method. Obtained results for surface area and pore diameter both range in typical values for MCM-41, regarding literature.[19,25,64] Comparing the properties of produced MCM-41 to ones obtained by *Tao et al.*, it can be concluded that this material satisfies the requirements for mesoporous nanostructured silica and can be used for immobilization attempts.[64]

2.3.2 Synthesis and characterization of SBA-15

SBA-15 nanostructures were synthesized following common procedure reported in literature before.[23] Briefly, Pluronic P123® was completely dissolved in a mixture of 2M HCl and water with subsequent addition of TEOS. Due to electrostatic interactions with the SDA, silica network is developing by hydrolysis and condensation, thereby forming SBA-15. The white solid material was obtained after filtration, washing with ethanol and further calcination. Produced MSNs were characterized using SEM, DLS and BET-analysis. SEM measurement displayed in Figure 16 reveals rod-shaped particles with sizes ranging between 760 – 910 nm as well as high homogeneity present in the prepared SBA-15. This size can be confirmed using DLS measurements (Figure A16). Obtained particles provide shape and size typical for SBA-15 according to literature, hence possessing sufficient properties for usage as carrier in immobilization attempts evaluated in this work.[23,64]

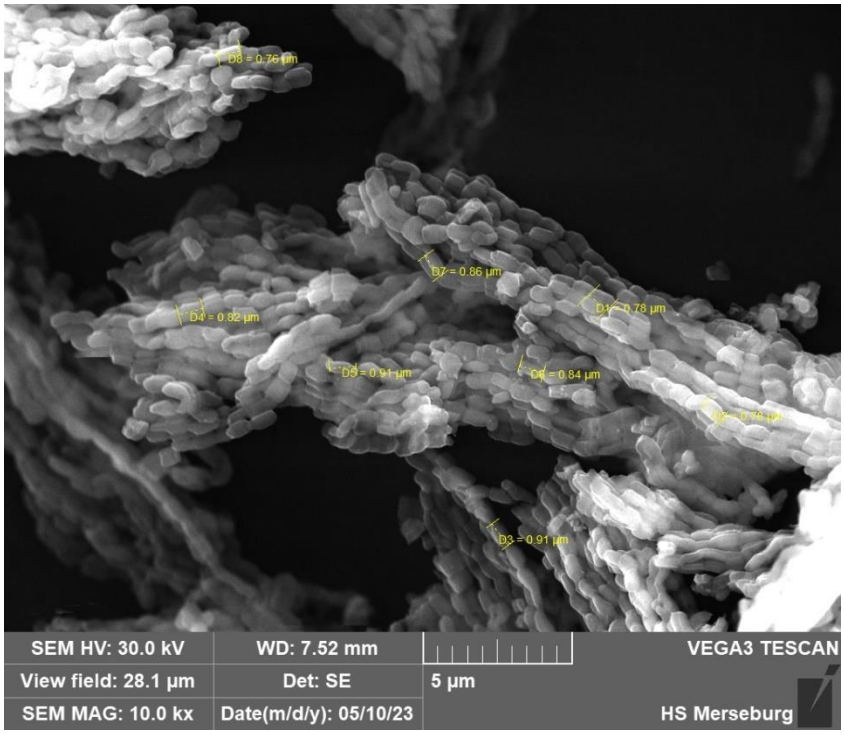

Figure 16: SEM of SBA-15

Nitrogen sorption measurements revealed isotherms of SBA-15 shown in Figure 17, which can be categorised to type IV(a) according to IUPAC.[65] Similar to obtained results of MCM-41 described previously, isotherms of prepared SBA-15 can be divided into three sections as well, displaying mono- and multilayer adsorption in pores occurring at low p/p_0 values (1), capillary condensation with hysteresis loop (2) as well as surface mono- and multilayer adsorption taking place at higher relative pressures. Providing a hysteresis loop with adsorption and

desorption happening time displaced, filling and release of gas from the pores occurs at different relative pressures in SBA-15. Thus indicating a pore size above 4 nm, the hysteresis loop displayed is characteristic for SBA-15 nanoparticles according to literature.[23,64,65] Specific surface area and pore diameter values were calculated using multi-point BET and BJH-method respectively, resulting in values of 658.3 $m^2 \cdot g^{-1}$ for area and a diameter of 5.05 nm. SBA-15 also satisfies the requirements for mesoporous nanostructured silica and can be used for immobilization attempts within the scope of this work.[23,64]

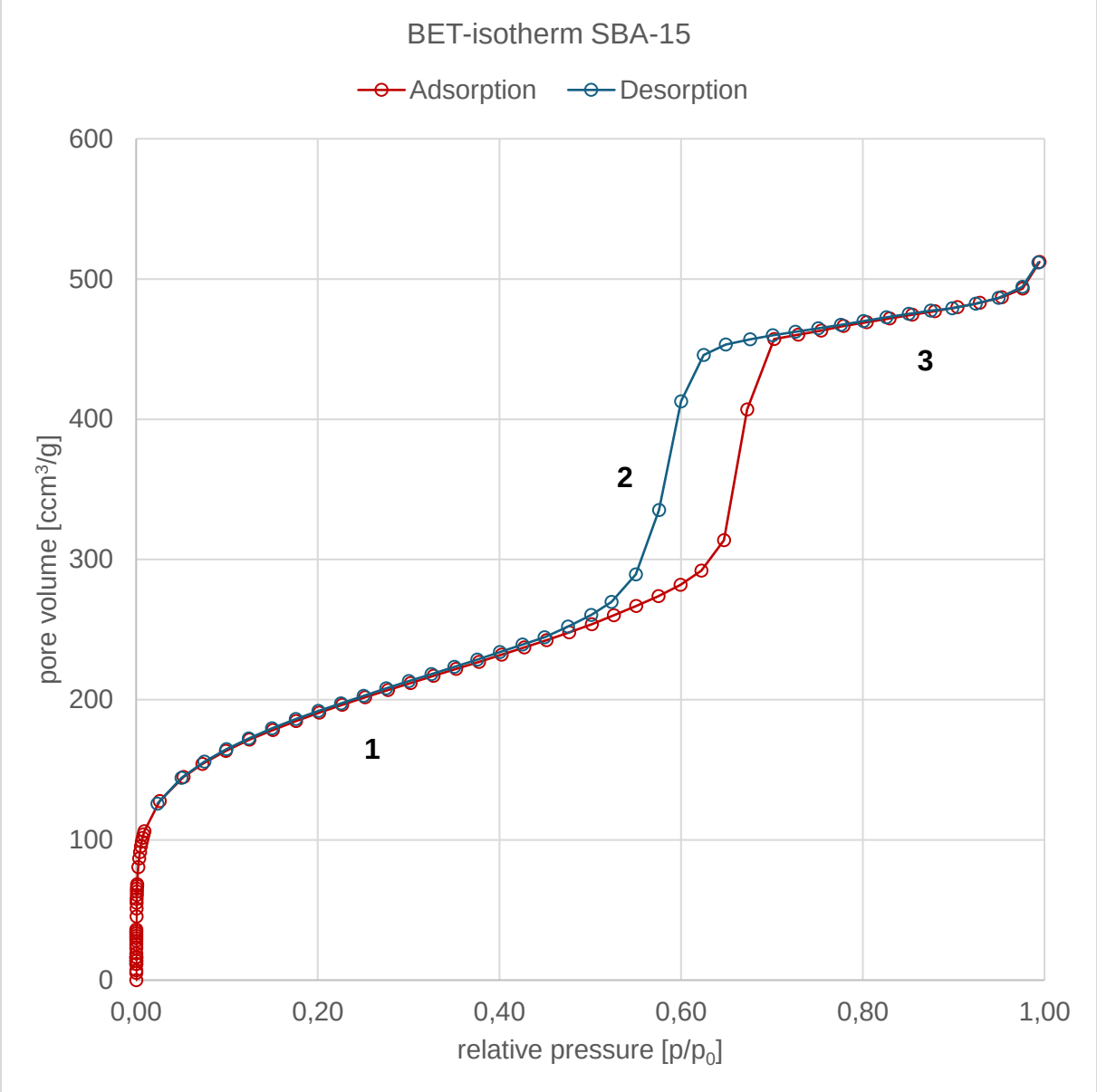

Figure 17: Adsorption and desorption isotherms of N_2 at 77 K for SBA-15

2.4 Immobilization of [(η^6-*p*-cym)Ru(L)Cl] (L^- = $L1^-$, $HL2^-$, $L3^-$) complexes into mesoporous nanostructured silica

Mesoporous nanostructured silica MCM-41 and SBA-15 were used as prepared for immobilization. Firstly, MSNs have to be activated at 150 °C under vacuum to remove any trapped water. Subsequently complexes **1 – 3** are dissolved in toluene and added to the MSNs under inert atmosphere. Immobilization was performed following literature while stirring the suspension for 48 h at 80 °C.[23] Since first attempts of immobilization lead to a severe change of colour from bright red to dark green while stirring in heat, the degradation of the used complex **1** due to too high temperatures was assumed. After adjusting the procedure to lower temperatures (20 °C) and therefore longer time (96 h) a light red solid could be obtained after filtering and washing with toluene and *n*-pentane (Figure A17). Therefore, the adjusted procedure was used to immobilize the complexes on both MSNs, preparing the six loaded MSNs MCM-41|**1–3** and SBA-15|**1–3**.

To determine amount of complex loaded into MSNs, energy dispersive X-ray spectroscopy (EDX) was performed. Results are shown in Table 1. It can be seen, that loaded amount of ruthenium determined in all MCM-41 compounds differs only little around 26.5 *w%*. In SBA-15 materials **1–3** were immobilized from 21.05–31.26 *w%*, with highest amount for **2**.

*Table 1: EDX results of ruthenium content (w%) in loaded MSNs MCM-41|**1–3** and SBA-15|**1–3***

Compound	*w%* (Ru)	Compound	*w%* (Ru)
MCM-41|**1**	**26.48**	SBA-15|**1**	**21.89**
MCM-41|**2**	**26.97**	SBA-15|**2**	**31.26**
MCM-41|**3**	**26.18**	SBA-15|**3**	**21.05**

Using EDX results, total mass and molar mass of the compound, the experimental loading of the compounds is calculated. The theoretically possible load can be calculated using the initial masses of used complex and MSNs. The loading efficiency is hence the ratio of experimental to theoretical loading. The calculated results are shown in Table 2.

The loading efficiency of **1** is higher in both species compared to other materials, showing the highest values into MCM-41 (Table 2). Loading efficiency values are in the range of 57.02–103.91%. Efficiency of SBA-15|**2** is showing result of more than 100 % (Table 2), however taking in consideration limitation of EDX also this value might be considered as representative.

Complex **3** is displaying the lowest immobilization into both MSNs, still revealing good loading into MCM-41 with 75.6 %. Adsorption in pores is depending on structure and shape of pores and the adsorbed compound, leading to differing loading efficiency. Regarding higher

efficiencies of complex **1** in comparison to **3**, it may be assumed that stereochemically smaller complexes adsorb better into the mesopores of used particles. Providing only one hydrogen atom bound to C3, the ligand moiety of **1** is taking less space than more voluminous acid and ester substitutes in **2** and **3**. Furthermore all complexes tend to show higher loading into MCM-41 in comparison to SBA-15. This is indicating that pore size and shape of MCM-41 particles is fitting adsorption requirements of used complexes better. Nevertheless, all materials showed high ruthenium content in MSNs justifying their usage in forthcoming biological studies.[23]

*Table 2: Theoretical/experimental loading and loading efficiency of compounds MCM-41|**1–3** and SBA-15|**1–3***

Compound	Loading (exp.) [mmol/g]	Loading (theo.) [mmol/g]	Loading efficiency [%]
MCM-41|**1**	0.907	1.004	**90.38**
MCM-41|**2**	0.837	0.998	**83.94**
MCM-41|**3**	0.756	1.000	**75.65**
SBA-15|**1**	0.706	0.986	**71.61**
SBA-15|**2**	1.032	0.993	**103.91**
SBA-15|**3**	0.569	0.997	**57.02**

To ensure that no degradation of the nanostructured silica is happening upon the immobilization process, SEM imaging of MSN|**1–3** was performed (Figure 18). It can be seen that the characteristic spherical or rod shape of the MSNs is retained in all samples, which point out that immobilization is not leading to destruction of the solid silica structure, retaining the characteristic properties of MSNs.

In conclusion, the loading of organoruthenium(II) compounds **1–3** on MCM-41 and SBA-15 carriers was proven to be successful, providing high loading efficiencies especially for complex **1**, in general showing higher results for loading on MCM-41 particles.

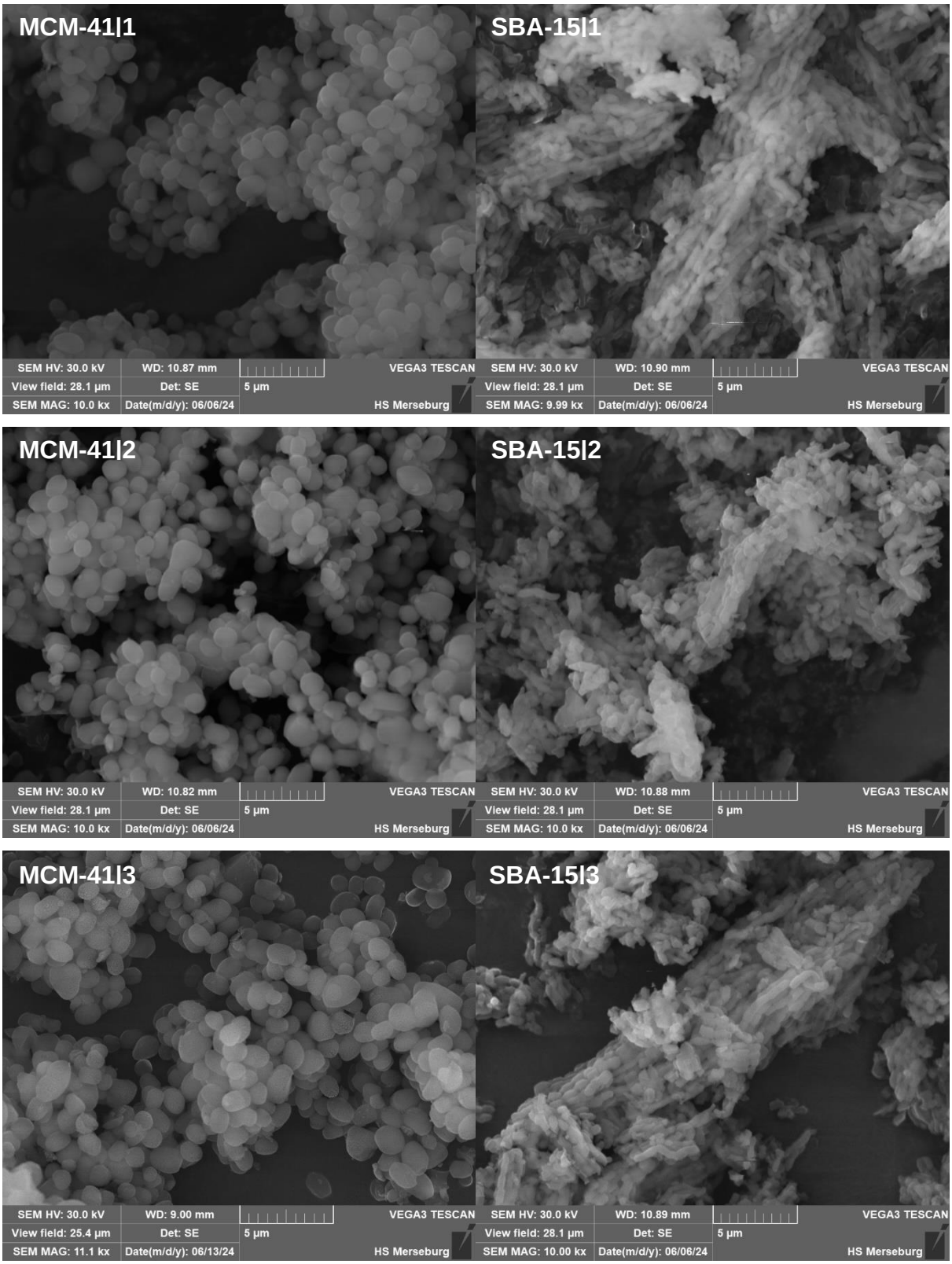

*Figure 18: SEM of MSNs: MCM-41|**1–3** and SBA-15|**1–3***

3 Conclusion

The interest in organoruthenium(II) compounds as potential outstanding candidates for cancer therapy is rising over the past decades, providing high cytotoxicity and selectivity with less side-effects in comparison to established chemotherapeutics. Nonetheless, still affecting healthy tissue and remaining with not sufficiently clarified binding mode towards DNA, their usage in clinical therapy is not yet established. Low solubility and stability in aqueous solutions lead to low bioavailability thus requiring high doses to achieve the desired therapeutic effect.

Among bioactive organoruthenium(II) compounds, complexes with arene ligands such as *p*-cym exhibit enhanced stability in aqueous solution improving their bioavailability. With evidence that pyrithione ligands were proven to increase the accumulation of transition metal ions in cells, a coordination of pyrithione to (η^6-arene)ruthenium(II) complexes is likely to combine increased bioavailability with enhanced cytotoxicity due to accumulation of ruthenium(II) inside malignant cells. Thus research on [(*p*-cym)Ru(pyrithione)Cl] complexes and its derivatives could lead to prominent alternatives of common chemotherapeutics.

Mesoporous nanostructured silica particles like MCM-41 and SBA-15 were shown to provide great properties for usage as drug delivery systems, providing high surface area, *in vivo* biocompatibility and highly adjustable parameters like size and shape. Moreover, accumulating preferably in tumour sites, MSNs turn out to be excellent carriers for anticancer therapy. The loading of novel transition metal-based drugs into MSNs hence can be beneficial for overcoming common problems of bioactive drugs like solubility and *in vivo* stability, resulting in better bioavailability.

Within the scope of this work the three complexes [(η^6-*p*-cym)Ru(**L**)Cl] (**L**$^-$ = **L1**$^-$**, HL2**$^-$, **L3**$^-$; **1–3**, respectively) were successfully synthesized and characterized, two of them (**1** and **2**) were already known from the literature.[52,61] Thereby the characterization of **L3** and **3** was performed using ^{1}H and ^{13}C NMR spectroscopy and purity was confirmed with elemental analysis. Evaluation of complex **2** lead to the assumption of a coordination mode through (C^2)*S*,(C^7*O*)*O* fashion of **HL2**$^-$, requiring further investigation.

Prepared organoruthenium(II) complexes were subsequently immobilised into two mesoporous nanostructured silica species MCM-41 and SBA-15. Loaded materials were analysed revealing high ruthenium contents of 21.0–26.1 *w*% and calculated loading efficiencies of 57.0–104.0 %. Upon loading of **1**–**3** particles remained without alterations in shape and morphology.

Obtained results reveal successful loading of prepared organoruthenium(II) compounds highlighting their potential use for subsequent biological studies related to the anticancer activity.

4 Experimental part

4.1 Materials and methods

Reactions for synthesis of ligands **H_2L2**, **HL3**, complexes **1–3** as well as particles MCM-41 and SBA-15 were performed under ambient conditions. Immobilization of compounds into mesoporous silica nanoparticles was performed under nitrogen atmosphere using standard Schlenk technique. Staring materials including **L1** were commercially available and used as purchased: tetraethylorthosilicate (99 %, Sigma Aldrich), cetyltrimethylammonium bromide (98%, abcr), Pluronic P123® (Sigma Aldrich), pyrithione (**L1**; Fluorochem), M2CN (98 %, TCI), TFAA (99 %, Roth), UHP (Roth), [{Ru(*p*-cymene)Cl_2}$_2$] (95 %, TCI), NaOMe (TCI), DCM (99.5 % Roth), ethanol (96 % Roth), toluene (99 % Roth), *n*-hexane (95 % Roth), *n*-pentane (95 % Roth)

4.1.1 Characterization of intermediaries, ligands and ruthenium(II) complexes

Synthesized compounds were characterized using multinuclear ^{1}H and ^{13}C NMR spectroscopy on a Bruker AVANCE DRX 400 (University of Applied Sciences Merseburg) or Bruker AVANCE III 600 spectrometer (University of Ljubljana). Spectra were recorded using $CDCl_3$ and DMSO-d_6 as solvent. Spectra ^{1}H (400.131 or 600.13 MHz) and ^{13}C (100.63 or 150.90 MHz) are referred to tetramethylsilane as internal standard or resident solvent peaks. Elemental analysis was performed using Thermo Scientific FlashSmart CHNS.

4.1.2 Characterization of mesoporous nanostructured silica

Scanning electron microscopy and energy dispersive X-ray spectroscopy were performed on a TESCAN VEGA 3 microscope with attached X-ray detector from EDAX APEX Inc. Dynamic light scattering was performed in aqueous solution using Malvern Panalytical Zetasizer Ultra. Brunauer-Emmet-Teller physisorption and sample outgassing (350 °C, 3 h) was performed on Autosorb iQ/ASiQwin from Quantochrome Instruments.

4.2 Synthesis of pyrithione-derived ligands (H_2L2 and HL3)

4.2.1 Synthesis of I1 (oxidation)

For the synthesis of **I1** 11.656 mmol (2 g) of M2CN were dissolved with two molar eq. (2.19 g) of UHP in 40 mL of DCM. Subsequently 23.312 mmol (4.896 g) of TFAA were added while stirring in ice. The reaction mixture was then stirred for at least 4 h at room temperature. Afterwards the solution was quenched with 25 mL of 2.0 M HCl and organic phase separated. The aqueous phase was extracted with 15 mL of DCM. Combined organic phases were washed twice using 100 mL of saturated $NaHCO_3$ solution and subsequently dried over

Na_2SO_4. Aqueous phases are extracted with 15 mL DCM. After filtration and evaporation of the solvent a solid is obtained.

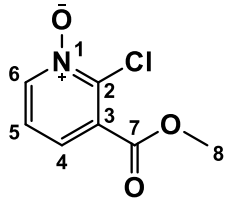

Yellow-white solid, $C_7H_6ClNO_3$, M_r = 187.58 $g \cdot mol^{-1}$

Yield: 1.588 g (72.6 %)

^{1}H NMR (600 MHz, $CDCl_3$) δ [ppm]: 8.45 (dd, $^3J_{HH}$ = 6.5, 1.5 Hz, 1H, C^4*H*), 7.66 (dd, $^3J_{HH}$ = 8.0, 1.5 Hz, 1H, C^6*H*), 7.26 (t, 1H, C^5*H*), 3.98 (s, 3H, C^8*H*$_3$).

4.2.2 Synthesis of H_2L2 (thiolation)

For preparation of **H_2L2** 8.5 mmol (1.6 g) of the oxidation product **I1** were dissolved with 10.2 mmol (0.774 g, 1.2 molar eq.) of thiourea in 80 mL of EtOH. The mixture was subsequently heated up to 80 °C and left to stir under reflux for 6 h. Afterwards the precipitating yellow intermediate product is filtered and dried overnight. Furthermore, the intermediate was dissolved with half molar eq. (0.248 g) of K_2CO_3 in 12.5 mL dest. water and a solution of 10.773 mmol (0.431 g) of NaOH in 12.5 mL dest. water was added. The alkaline solution was heated up to 80 °C and stirred for 1.5 h. Subsequently concentrated HCl was added until pH = 1, leading to precipitation of the product. Obtained solid was filtered and dried overnight.

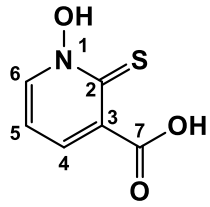

Yellow solid, $C_6H_5NO_3S$, M_r = 171.17 $g \cdot mol^{-1}$

Yield = 0.663 g (45.7 %)

^{1}H NMR (600 MHz, DMSO-d6) δ [ppm]: 14.27 (bs, 1H, C^{7}OO*H* or N-O*H*), 13.11 (bs, 1H, C^{7}OO*H* or N-O*H*), 8.70 (dd, $^3J_{HH}$ = 6.5, 1.5 Hz, 1H, C^4*H*), 8.12 (dd, $^3J_{HH}$ = 7.5, 1.5 Hz, 1H, C^6*H*), 7.04 (t, 1H, C^5*H*).

^{13}C NMR (151 MHz, DMSO-d6) δ [ppm]: 167.9 (*C*OOH, *C*^{7}) 165.6 (*C*H, *C*^{2}), 139.8 (*C*H, *C*^{4}), 136.6 (*C*H, *C*^{6}), 133.3 (*C*H, *C*^{3}), 113.5. (*C*H, *C*^{5}).

Elemental analysis: calculated (%) for $C_6H_5NO_3S$: C, 42.10; H, 2.94; N, 8.18; found: C, 42.10; H, 2.76; N, 8.39

4.2.3 Synthesis of HL3 (esterification)

For synthesis of **HL3** firstly 120 mL of EtOH were stirred in ice, afterwards 7.008 mmol (0.834 g) of $SOCl_2$ was added dropwise over 30 min. 1.168 mmol (0.2 g) of **H_2L2** was dissolved in the mixture and continuously stirred for 2 h at 0 °C. Subsequently the solution is heated up under reflux at 80 °C for 6 h and the solvent is evaporated. The product was purified using

silica column chromatography with 2 % MeOH in DCM as mobile phase. First fraction obtained contained the pure product. After evaporation of the mobile phase, **HL3** was yielded as solid.

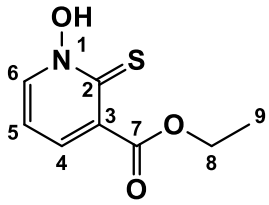

Green-brown solid, $C_8H_9NO_3S$, M_r = 199.22 $g \cdot mol^{-1}$

Yield = 0.139 g (59.9 %)

^{1}H NMR (400 MHz, DMSO-d6) δ [ppm]: 12.59 (bs, 1H, N-O*H*), 8.64 (dd, $^3J_{HH}$ = 6.8, 1.6 Hz, 1H, C^4*H*), 7.73 (dd, $^3J_{HH}$ = 7.4, 1.6 Hz, 1H, C^6*H*), 6.95 (t, 1H, C^5*H*), 4.28 (q, $^3J_{HH}$ = 7.1 Hz, 2H, C^{7}OO-C*H*$_2$-CH$_3$), 1.29 (t, $^3J_{HH}$ = 7.1 Hz, 3H, C^{7}OO-CH$_2$-C*H*$_3$).

^{13}C NMR (101 MHz, DMSO) δ [ppm]: 166.0 (*C*OOEt, *C*^{7}), 165.3 (*C*H, *C*^{2}), 136.8 (*C*H, *C*^{4}), 135.63 (*C*H, *C*^{6}), 133.4 (*C*H, *C*^{3}), 112.9 (*C*H, *C*^{5}), 61.50 (t, $^1J_{CH}$ = 4.9 Hz, -*C*H$_2$-CH$_3$, *C*^{8}), 14.0 (d, $^1J_{CH}$ = 2.9 Hz, -CH$_2$-*C*H$_3$, *C*^{9}).

Elemental analysis: calculated (%) for $C_8H_9NO_3S$: C, 48.23; H, 4.55; N, 7.03; S, 16.09; found: C, 48.38; H, 4.54; N, 7.22; S, 16.46

4.3 Synthesis of [(*p*-cym)Ru(L)Cl] (L$^-$ = L1$^-$, HL2$^-$, L3$^-$) complexes (1–3)

4.3.1 Synthesis of [(η^6-*p*-cym)Ru(L1)Cl] (1)

Complex **1** was prepared following procedure reported in literature.[52] Briefly, 0.252 mmol (0.154 g) of [{Ru(*p*-cymene)Cl$_2$}$_2$] were dissolved with two molar eq. (0.064 g) of commercially available **L1** and two eq. (0.027 g) of NaOMe in 50 mL of DCM and stirred for 2 h. Afterwards the solvent was evaporated and the product purified using a celite flash column with DCM as mobile phase. Subsequently the mobile phase was evaporated and the solid again dissolved in 2 mL of DCM. Furthermore, 30 mL of *n*-hexane were added rapidly, leading to precipitation of the product.

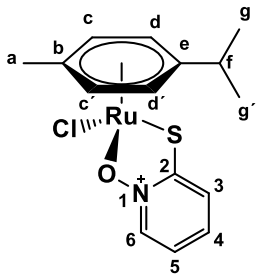

Blood-red solid, $C_{15}H_{18}ClNORuS$, M_r = 396.89 $g \cdot mol^{-1}$

Yield = 0.2 g (99.9 %)

^{1}H NMR (400 MHz, $CDCl_3$) δ [ppm]: 8.03 (d, $^3J_{HH}$ = 6.6 Hz, 1H, C^3*H*), 7.44 (d, $^3J_{HH}$ = 8.2 Hz, 1H, C6-*H*), 7.03 (t, $^3J_{HH}$ = 7.6 Hz, 1H, C^4*H*), 6.71 (td, $^3J_{HH}$ = 6.8, 1.6 Hz, 1H, C^5*H*), 5.47 (d, $^3J_{HH}$ = 5.8 Hz, 2H, C$^{c,c´}$*H*), 5.26 (d, $^3J_{HH}$ = 5.7 Hz, 2H, C$^{d,d´}$*H*), 2.82 (hept, $^3J_{HH}$ = 6.9 Hz, 1H, C^e-C*H*(CH$_3$)$_2$), 2.24 (s, 3H, C^b-C*H*$_3$), 1.26 (d, $^3J_{HH}$ = 6.9 Hz, 6H, C^e-CH(C*H*$_3$)$_2$).

^{13}C NMR (101 MHz, $CDCl_3$) δ [ppm]: 160.7 (*C*H, C^2), 137.2 (*C*H, C^4), 129.5 (*C*H, C^6), 127.8 (*C*H, C^3), 117.5 (*C*H, C^5), 100.7 (*C*-CH(CH_3)$_2$, C^e), 98.7 (*C*H-CH_3, C^b), 82.4 (*C*H, $C^{c,c'}$), 81.1 (*C*H, $C^{d,d'}$), 31.0 (C-*C*H(CH_3)$_2$, C^f), 22.6 (C-CH(*C*H_3)$_2$, $C^{g,g'}$), 18.6 (d, $^1J_{CH}$ = 4.1 Hz, C-*C*H_3, C^a).

Elemental analysis: calculated (%) for $C_{15}H_{18}ClNORuS$: C, 45.39; H, 4.57; N, 3.53; S, 8.08; found: C, 44.88; H, 4.54; N, 3,08; S, 8.08

4.3.2 Synthesis of [(η^6-*p*-cym)Ru(HL2)Cl] (2)

Complex **2** was prepared following procedure reported in literature.[52] Firstly, 0.227 mmol (0.139 g) of [{Ru(*p*-cymene)Cl_2}$_2$] were dissolved with two molar eq. (0.078 g) of **H_2L2** and two eq. (0.025 g) of NaOMe in 50 mL of DCM and stirred for 2 h. Afterwards the solvent was evaporated and the product purified using a celite flash column with DCM as mobile phase. Subsequently the mobile phase was evaporated and the solid again dissolved in 2 mL of DCM. Furthermore, 30 mL of *n*-hexane were added rapidly, leading to precipitation of the product.

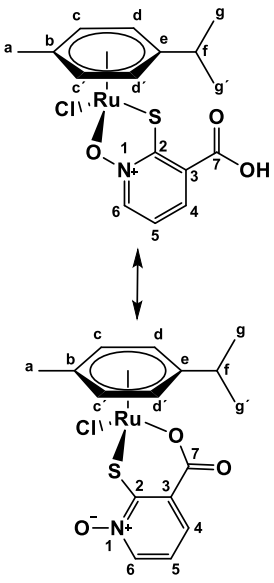

Red solid, $C_{16}H_{18}ClNO_3RuS$, M_r = 440.90 $g \cdot mol^{-1}$

Yield = 0.134 g (67.0 %)

^{1}H NMR (600 MHz, $CDCl_3$) δ [ppm]: 8.21 (dd, $^3J_{HH}$ = 6.4, 1.2 Hz, 1H, C^4H), 7.92 (dd, $^3J_{HH}$ = 7.7, 1.4 Hz, 1H, C^6H), 6.82 (t, 1H, C^5H), 5.53 (d, $^3J_{HH}$ = 6.1 Hz, 2H, $C^{c,c'}H$), 5.31 (d, $^3J_{HH}$ = 6.1 Hz, 2H, $C^{d,d'}H$), 2.83 (hept, $^3J_{HH}$ = 7.1 Hz, 1H, C^e-C*H*(CH_3)$_2$), 2.24 (s, 3H, C^b-CH_3), 1.28 (d, $^3J_{HH}$ = 6.9 Hz, 6H, C^e-CH(CH_3)$_2$).

^{13}C NMR (101 MHz, $CDCl_3$) δ [ppm]: 166.5 (*C*OOH, C^7), 163.3 (*C*H, C^2), 140.6 (*C*H, C^4), 134.5 (*C*H, C^6), 128.9 (*C*H, C^3), 116.5 (*C*H, C^5), 101.3 (*C*-CH(CH_3)$_2$, C^e), 98.8 (*C*-CH_3, C^b), 82.9 (*C*H, $C^{c,c'}$), 81.7 (*C*H, $C^{d,d'}$), 31.0 (C-*C*H(CH_3)$_2$, *Cf*), 22.6 (C-CH(*C*H_3)$_2$, $C^{g,g'}$), 18.7 (d, $^1J_{CH}$ = 3.3 Hz, C-*C*H_3, C^a).

Elemental analysis: calculated (%) for $C_{16}H_{18}ClNO_3RuS$: C, 43.59; H, 4.12; N, 3.18; found: C, 43.86; H, 3.66; N, 3.29

4.3.3 Synthesis of [(η^6-*p*-cym)Ru(L3)Cl] (3)

Complex **3** was prepared following procedure reported in literature.[52] Briefly, 0.213 mmol (0.131 g) of [{Ru(*p*-cymene)Cl_2}$_2$] were dissolved with two molar eq. (0.085 g) of **HL3** and two

eq. (0.023 g) of NaOMe in 50 mL of DCM and stirred for 2 h. Afterwards the solvent was evaporated and the product purified using a celite flash column with DCM as mobile phase. Subsequently the mobile phase was evaporated and the solid again dissolved in 2 mL of DCM. Furthermore, 30 mL of *n*-hexane were added rapidly, leading to precipitation of the product.

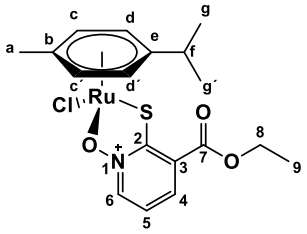

Dark-red solid, $C_{18}H_{22}ClNO_3RuS$, M_r = 468.96 $g \cdot mol^{-1}$

Yield = 0.166 g (83.0 %)

^{1}H NMR (400 MHz, $CDCl_3$) δ [ppm]: 8.15 (dd, $^3J_{HH}$ = 6.6, 1.5 Hz, 1H, C^4*H*), 7.75 (dd, $^3J_{HH}$ = 7.6, 1.4 Hz, 1H, C^6*H*), 6.74 (t, 1H, C^5*H*), 5.49 (d, $^3J_{HH}$ = 5.8 Hz, 2H, C$^{c,c´}$*H*), 5.27 (d, $^3J_{HH}$ = 5.8 Hz, 2H, C$^{d,d´}$*H*), 4.38 (q, $^3J_{HH}$ = 7.1 Hz, 2H, C^{7}OO-C*H*$_2$-CH$_3$), 2.82 (hept, $^3J_{HH}$ = 6.8 Hz, 1H, C^e-C*H*(CH$_3$)$_2$), 2.21 (s, 3H, C^b-C*H*$_3$), 1.38 (t, $^3J_{HH}$ = 7.1 Hz, 3H, C^{7}OO-CH$_2$-C*H*$_3$), 1.27 (d, $^3J_{HH}$ = 6.9 Hz, 6H, C^e-CH(C*H*$_3$)$_2$).

^{13}C NMR (101 MHz, $CDCl_3$) δ [ppm]: 164.1 (*C*OO-CH$_2$-CH$_3$, *C*^{7}), 163.5 (*C*H, *C*^{2}), 139.9 (*C*H, *C*^{4}), 133.0 (*C*H, *C*^{6}), 129.7 (*C*H, *C*^{3}), 115.9 (*C*H, *C*^{5}), 101.0 (*C*-CH(CH$_3$)$_2$, *C*^{e}), 98.5 (*C*-CH$_3$, *C*^{b}), 85.9 – 79.2 (m, *C*H, *C*$^{c,c´}$; *C*$^{d,d´}$), 62.0 (COO-*C*H$_2$-CH$_3$, *C*^{8}), 31.0 (C-*C*H(CH$_3$)$_2$, *C*^{f}), 22.7 (C-CH(*C*H$_3$)$_2$, *C*^{g,g}), 18.6 (d, $^1J_{CH}$ = 4.2 Hz, C-*C*H$_3$, *C*^{a}), 14.4 (d, ^1J_H = 2.6 Hz, COO-CH$_2$-*C*H$_3$, *C*^{9}).

Elemental analysis: calculated (%) for $C_{18}H_{22}ClNO_3RuS$: C, 46.10; H, 4.73; N, 2.99; S, 6.84; found: C, 46.45; H, 4.87; N, 2.47; S, 6.76

4.4 Synthesis of MCM-41

MCM-41 was synthesized using slightly adjusted literature procedure.[64] Briefly, 5.5 mmol (4 g) CTAB were dissolved in 480 mL of dest. water and stirred at 35 °C until completely dissolved. Afterwards, the solution is heated up to 75 °C with subsequent addition of 7 mL 2.0 M NaOH solution. Further 50.6 mmol (10.54 g) TEOS were added dropwise into the solution, subsequently stirring for 2 h at 75 °C (350 – 700 rpm). The product is filtered when still hot and washed with app. 300 mL of distilled water and 300 mL EtOH. Obtained white solid was dried overnight at 80 °C. Removal of surfactant template was carried out using calcination at 550 °C for 5 h with heating rate of 1 $°C \cdot min^{-1}$ yielding MCM-41.

Yield: 2.46 g (80.9 %)

Specific surface Area (BET): 1005.7 $m^2 \cdot g^{-1}$

Pore Volume (BJH): 0.126 $cm^3 \cdot g^{-1}$

Pore diameter (BJH): 3.11 nm

4.5 Synthesis of SBA-15

SBA-15 was prepared with downscaled reported literature procedure.[23] In detail, 8 g of Pluronic-123® were dissolved in prewarmed mixture of 60 mL dest. water and 240 mL of 2.0 M HCl at 35 °C under reflux until clear solution was formed. Afterwards, 81.6 mmol (17.0 g) of TEOS is added dropwise and the solution is stirred vigorously (700 rpm) for 20 h at 35 °C and additionally stirred for 24 h at 80 °C. Subsequently 20 mL of EtOH is added and the mixture is filtered when still hot. After washing with 500 mL distilled water, the white product is dried overnight at 90 °C and further calcined at 500 °C for 24 h with heating rate of 1 $°C \cdot min^{-1}$.

Yield: 4,71 g (96.0 %)

Specific surface Area (BET): 658.3 $m^2 \cdot g^{-1}$

Pore Volume (BJH): 0.686 $cm^3 \cdot g^{-1}$

Pore diameter (BJH): 5.05 nm

4.6 Immobilization of 1–3 into MSNs

For preparation of loaded drugs MCM-41|**1–3** and SBA-15|**1–3** procedure reported in literature for other metal complexes was slightly modified.[23] Briefly, 0.2 mmol of complexes **1–3** were pulverized in an achat mortar, suspended in 30 mL of toluene and further added to 0.2 g of the

MSN material, previously pulverized and activated by drying under vacuum at 150 °C for 16 h. The forming suspension was stirred at room temperature for 96 h under inert atmosphere. After completion, the obtained material was isolated by filtration over a G4 frit without pressure, followed by successive washing with toluene and *n*-pentane. Prepared light red MSNs were dried at room temperature.

MCM-41|1: 79.9 mg of **1**, 200.5 mg of MCM-41; **Yield: 276.7 mg** (98.7 %) **EDX: 26.48 *w*% Ru**

MCM-41|2: 88.5 mg of **2**, 201.2 mg of MCM-41; **Yield: 284.8 mg** (98.3 %) **EDX: 27.97 *w*% Ru**

MCM-41|3: 93.9 mg of **2**, 200.3 mg of MCM-41; **Yield: 250.8 mg** (85.3 %) **EDX: 26.18 *w*% Ru**

SBA-15|1: 79.3 mg of **1**, 200.2 mg of SBA-15; **Yield: 278.8 mg** (99.8 %) **EDX: 21.89 *w*% Ru**

SBA-15|2: 88.2 mg of **2**, 201.5 mg of SBA-15; **Yield: 254.0 mg** (87.7 %) **EDX: 31.26 *w*% Ru**

SBA-15|3: 93.8 mg of **3**, 200.6 mg of SBA-15; **Yield: 220.7 mg** (75.0 %) **EDX: 21.05 *w*% Ru**

5 References

1. Rosenberg, B., van Camp, L., and Krigas, T., “Inhibition of Cell Division in Escherichia coli by Electrolysis Products from a Platinum Electrode,” *Nature*, V. 205, 1965, pp. 698–699.
2. Anthony, E. J., Bolitho, E. M., Bridgewater, H. E., Carter, O. W. L., Donnelly, J. M., Imberti, C., Lant, E. C., Lermyte, F., Needham, R. J., Palau, M., Sadler, P. J., Shi, H., Wang, F.-X., Zhang, W.-Y., and Zhang, Z., “Metallodrugs are unique: opportunities and challenges of discovery and development,” *Chemical Science*, V. 11, No. 48, 2020, pp. 12888–12917.
3. Rosenberg, B., van Camp, L., Trosko, J. E., and Mansour, V. H., “Platinum compounds: a new class of potent antitumour agents,” *Nature*, V. 222, No. 5191, 1969, pp. 385–386.
4. Ghosh, S., “Cisplatin: The first metal based anticancer drug,” *Bioorganic Chemistry*, V. 88, 2019, p. 102925.
5. Fuertes, M. A., Alonso, C., and Pérez, J. M., “Biochemical modulation of Cisplatin mechanisms of action: enhancement of antitumor activity and circumvention of drug resistance,” *Chemical Reviews*, V. 103, No. 3, 2003, pp. 645–662.
6. Jamieson, E. R., and Lippard, S. J., “Structure, Recognition, and Processing of Cisplatin-DNA Adducts,” *Chemical Reviews*, V. 99, No. 9, 1999, pp. 2467–2498.
7. Siddik, Z. H., “Cisplatin: mode of cytotoxic action and molecular basis of resistance,” *Oncogene*, V. 22, No. 47, 2003, pp. 7265–7279.
8. Barabas, K., Milner, R., Lurie, D., and Adin, C., “Cisplatin: a review of toxicities and therapeutic applications,” *Veterinary and Comparative Oncology*, V. 6, No. 1, 2008, pp. 1–18.
9. Iwasaki, Y., Nagata, K., Nakanishi, M., Natuhara, A., Kubota, Y., Ueda, M., Arimoto, T., and Hara, H., “Double-cycle, high-dose ifosfamide, carboplatin, and etoposide followed by peripheral blood stem-cell transplantation for small cell lung cancer,” *Chest*, V. 128, No. 4, 2005, pp. 2268–2273.
10. Kosmas, C., Tsavaris, N. B., Malamos, N. A., Vadiaka, M., and Koufos, C., “Phase II study of paclitaxel, ifosfamide, and cisplatin as second-line treatment in relapsed small-cell lung cancer,” *Journal of Clinical Oncology*, V. 19, No. 1, 2001, pp. 119–126.
11. Muggia, F. M., and Los, G., “Platinum resistance: laboratory findings and clinical implications,” *Stem Cells*, V. 11, No. 3, 1993, pp. 182–193.
12. Kartalou, M., and Essigmann, J. M., “Mechanisms of resistance to cisplatin,” *Mutation Research*, V. 478, 1-2, 2001, pp. 23–43.
13. Brabec, V., and Kasparkova, J., “Modifications of DNA by platinum complexes. Relation to resistance of tumors to platinum antitumor drugs,” *Drug Resistance Updates*, V. 8, No. 3, 2005, pp. 131–146.

14. Lee, S. Y., Kim, C. Y., and Nam, T.-G., “Ruthenium Complexes as Anticancer Agents: A Brief History and Perspectives,” *Drug Design, Development and Therapy*, V. 14, 2020, pp. 5375–5392.
15. Nováková, O., Kaspárková, J., Vrána, O., van Vliet, P. M., Reedijk, J., and Brabec, V., “Correlation between cytotoxicity and DNA binding of polypyridyl ruthenium complexes,” *Biochemistry*, V. 34, No. 38, 1995, pp. 12369–12378.
16. Shi, S., Geng, X., Zhao, J., Yao, T., Wang, C., Yang, D., Zheng, L., and Ji, L., “Interaction of $Ru(bpy)_2(dppz)^{2+}$ with human telomeric DNA: preferential binding to G-quadruplexes over i-motif,” *Biochimie*, V. 92, No. 4, 2010, pp. 370–377.
17. Mahmud, K. M., Niloy, M. S., Shakil, M. S., and Islam, M. A., “Ruthenium Complexes: An Alternative to Platinum Drugs in Colorectal Cancer Treatment,” *Pharmaceutics*, V. 13, No. 8, 2021.
18. Trudu, F., Amato, F., Vaňhara, P., Pivetta, T., Peña-Méndez, E. M., and Havel, J., “Coordination compounds in cancer: Past, present and perspectives,” *Journal of Applied Biomedicine*, V. 13, No. 2, 2015, pp. 79–103.
19. Beck, M., “Mesoporöse Silikananopartikel als Transportsysteme für miRNA und Wirkstoffmoleküle für die Therapie von Krebsstammzellen,” Dissertation, Universität Ulm, Institut für Anorganische Chemie II, Ulm, 2017.
20. Nam, L., Coll, C., Erthal, L. C. S., La Torre, C. de, Serrano, D., Martínez-Máñez, R., Santos-Martínez, M. J., and Ruiz-Hernández, E., “Drug Delivery Nanosystems for the Localized Treatment of Glioblastoma Multiforme,” *Materials*, V. 11, No. 5, 2018.
21. Fathi Vavsari, V., Mohammadi Ziarani, G., and Badiei, A., “The role of SBA-15 in drug delivery,” *RSC Advances*, V. 5, No. 111, 2015, pp. 91686–91707.
22. Bharti, C., Nagaich, U., Pal, A. K., and Gulati, N., “Mesoporous silica nanoparticles in target drug delivery system: A review,” *International Journal of Pharmaceutical Investigation*, V. 5, No. 3, 2015, pp. 124–133.
23. Predarska, I., Saoud, M., Drača, D., Morgan, I., Komazec, T., Eichhorn, T., Mihajlović, M., Dundjerović, D., Mijatović, S., Maksimović-Ivanić, D., Hey-Hawkins, E., and Kaluđerović, G. N., “Mesoporous Silica Nanoparticles Enhance the Anticancer Efficacy of Platinum(IV)-Phenolate Conjugates in Breast Cancer Cell Lines,” *Nanomaterials*, V. 12, No. 21, 2022, pp. 3767–3790.
24. Gao, Y., Gao, D., Shen, J., and Wang, Q., “A Review of Mesoporous Silica Nanoparticle Delivery Systems in Chemo-Based Combination Cancer Therapies,” *Frontiers in Chemistry*, V. 8, 2020, p. 598722.
25. Watermann, A., “Evaluation of Mesoporous Silica Nanoparticles for Head and Neck Cancer Therapy,” Dissertation, Johannes Gutenberg University Mainz, Mainz, 2019, p. 189

26. Schubert, U., and Hüsing, N., “Synthesis of inorganic materials,” 2., rev. and updated ed., Wiley-VCH, Weinheim, 2005, p. 409
27. Fröhlich, E., “The role of surface charge in cellular uptake and cytotoxicity of medical nanoparticles,” *International Journal of Nanomedicine*, V. 7, 2012, pp. 5577–5591.
28. Jurkić, L. M., Cepanec, I., Pavelić, S. K., and Pavelić, K., “Biological and therapeutic effects of ortho-silicic acid and some ortho-silicic acid-releasing compounds: New perspectives for therapy,” *Nutrition & Metabolism*, V. 10, No. 1, 2013, p. 2.
29. Lin, Y.-S., and Haynes, C. L., “Impacts of mesoporous silica nanoparticle size, pore ordering, and pore integrity on hemolytic activity,” *Journal of the American Chemical Society*, V. 132, No. 13, 2010, pp. 4834–4842.
30. He, Q., Zhang, Z., Gao, F., Li, Y., and Shi, J., “In vivo biodistribution and urinary excretion of mesoporous silica nanoparticles: effects of particle size and PEGylation,” *Small*, V. 7, No. 2, 2011, pp. 271–280.
31. Lu, J., Liong, M., Li, Z., Zink, J. I., and Tamanoi, F., “Biocompatibility, biodistribution, and drug-delivery efficiency of mesoporous silica nanoparticles for cancer therapy in animals,” *Small*, V. 6, No. 16, 2010, pp. 1794–1805.
32. Krajnović, T., Maksimović-Ivanić, D., Mijatović, S., Drača, D., Wolf, K., Edeler, D., Wessjohann, L. A., and Kaluđerović, G. N., “Drug Delivery System for Emodin Based on Mesoporous Silica SBA-15,” *Nanomaterials*, V. 8, No. 5, 2018, p. 322.
33. Meng, H., Mai, W. X., Zhang, H., Xue, M., Xia, T., Lin, S., Wang, X., Zhao, Y., Ji, Z., Zink, J. I., and Nel, A. E., “Codelivery of an optimal drug/siRNA combination using mesoporous silica nanoparticles to overcome drug resistance in breast cancer in vitro and in vivo,” *ACS Nano*, V. 7, No. 2, 2013, pp. 994–1005.
34. Krejčová, P., Kučerová, P., Stafford, G. I., Jäger, A. K., and Kubec, R., “Antiinflammatory and neurological activity of pyrithione and related sulfur-containing pyridine N-oxides from Persian shallot (Allium stipitatum),” *Journal of Ethnopharmacology*, V. 154, No. 1, 2014, pp. 176–182.
35. Chandler, C. J., and Segel, I. H., “Mechanism of the antimicrobial action of pyrithione: effects on membrane transport, ATP levels, and protein synthesis,” *Antimicrobial Agents and Chemotherapy*, V. 14, No. 1, 1978, pp. 60–68.
36. Ding, W.-Q., and Lind, S. E., “Metal ionophores - an emerging class of anticancer drugs,” *IUBMB Life*, V. 61, No. 11, 2009, pp. 1013–1018.
37. “Commision Regulation (EU) No 2021/1902: amending Annexes II, III and V to Regulation (EC) No 1223/2009 of the European Parliament and of the Council as regards the use in cosmetic products of certain substances classified as carcinogenic, mutagenic or toxic for reproduction,” 2021.

38. Scientific Committee on Consumer Saftey SCCS, ed., “Opinion on Zinc Pyrithione (ZPT) (P81) CAS N° 13463-41-7 - submission III,” 2020.
39. Novilla, M. N., “Chapter 78 - Ionophores,” *Veterinary Toxicology (Third Edition)*, R. C. Gupta, ed., Academic Press, 2018, pp. 1073–1092.
40. Srivastava, G., Matta, A., Fu, G., Somasundaram, R. T., Datti, A., Walfish, P. G., and Ralhan, R., “Anticancer activity of pyrithione zinc in oral cancer cells identified in small molecule screens and xenograft model: Implications for oral cancer therapy,” *Molecular Oncology*, V. 9, No. 8, 2015, pp. 1720–1735.
41. Qiu, M., Chen, Y., Chu, Y., Song, S., Yang, N., Gao, J., and Wu, Z., “Zinc ionophores pyrithione inhibits herpes simplex virus replication through interfering with proteasome function and NF-κB activation,” *Antiviral Research*, V. 100, No. 1, 2013, pp. 44–53.
42. Rudolf, E., and Cervinka, M., “Zinc pyrithione induces cellular stress signaling and apoptosis in Hep-2 cervical tumor cells: the role of mitochondria and lysosomes,” *Biometals*, V. 23, No. 2, 2010, pp. 339–354.
43. Kladnik, J., Dolinar, A., Kljun, J., Perea, D., Grau-Expósito, J., Genescà, M., Novinec, M., Buzon, M. J., and Turel, I., “Zinc pyrithione is a potent inhibitor of PLPro and cathepsin L enzymes with ex vivo inhibition of SARS-CoV-2 entry and replication,” *Journal of Enzyme Inhibition and Medicinal Chemistry*, V. 37, No. 1, 2022, pp. 2158–2168.
44. Lebeau, A., “Platinum Group Elements: Palladium, Iridium, Osmium, Rhodium, and Ruthenium,” *Hamilton & Hardy's industrial toxicology*, Sixth edition, G. T. Johnson, M. M. Bourgeois, and R. D. Harbison, eds., Wiley, Hoboken, New Jersey, 2015, pp. 187–192.
45. Allardyce, C. S., and Dyson, P. J., “Ruthenium in Medicine: Current Clinical Uses and Future Prospects,” *Platinum Metals Review*, V. 45, No. 2, 2001, pp. 62–69.
46. Alessio, E., “Thirty Years of the Drug Candidate NAMI-A and the Myths in the Field of Ruthenium Anticancer Compounds: A Personal Perspective,” *European Journal of Inorganic Chemistry*, V. 2017, No. 12, 2017, pp. 1549–1560.
47. Brabec, V., and Nováková, O., “DNA binding mode of ruthenium complexes and relationship to tumor cell toxicity,” *Drug Resistance Updates*, V. 9, No. 3, 2006, pp. 111–122.
48. Trédan, O., Galmarini, C. M., Patel, K., and Tannock, I. F., “Drug resistance and the solid tumor microenvironment,” *Journal of the National Cancer Institute*, V. 99, No. 19, 2007, pp. 1441–1454.
49. Clarke, M. J., Zhu, F., and Frasca, D. R., “Non-platinum chemotherapeutic metallopharmaceuticals,” *Chemical Reviews*, V. 99, No. 9, 1999, pp. 2511–2534.
50. Novakova, O., Chen, H., Vrana, O., Rodger, A., Sadler, P. J., and Brabec, V., “DNA interactions of monofunctional organometallic ruthenium(II) antitumor complexes in cell-free media,” *Biochemistry*, V. 42, No. 39, 2003, pp. 11544–11554.

51. Novakova, O., Kasparkova, J., Bursova, V., Hofr, C., Vojtiskova, M., Chen, H., Sadler, P. J., and Brabec, V., “Conformation of DNA modified by monofunctional Ru(II) arene complexes: recognition by DNA binding proteins and repair. Relationship to cytotoxicity,” *Chemistry & Biology*, V. 12, No. 1, 2005, pp. 121–129.
52. Kljun, J., Anko, M., Traven, K., Sinreih, M., Pavlič, R., Peršič, Š., Ude, Ž., Codina, E. E., Stojan, J., Lanišnik Rižner, T., and Turel, I., “Pyrithione-based ruthenium complexes as inhibitors of aldo-keto reductase 1C enzymes and anticancer agents,” *Dalton Transactions*, V. 45, No. 29, 2016, pp. 11791–11800.
53. Rižner, T. L., and Penning, T. M., “Role of aldo-keto reductase family 1 (AKR1) enzymes in human steroid metabolism,” *Steroids*, V. 79, 2014, pp. 49–63.
54. Deng, H. B., Adikari, M., Parekh, H. K., and Simpkins, H., “Ubiquitous induction of resistance to platinum drugs in human ovarian, cervical, germ-cell and lung carcinoma tumor cells overexpressing isoforms 1 and 2 of dihydrodiol dehydrogenase,” *Cancer Chemotherapy and Pharmacology*, V. 54, No. 4, 2004, pp. 301–307.
55. Ristovski, S., Uzelac, M., Kljun, J., Lipec, T., Uršič, M., Zemljič Jokhadar, Š., Žužek, M. C., Trobec, T., Frangež, R., Sepčić, K., and Turel, I., “Organoruthenium Prodrugs as a New Class of Cholinesterase and Glutathione-S-Transferase Inhibitors,” *ChemMedChem*, V. 13, No. 20, 2018, pp. 2166–2176.
56. Kladnik, J., Kljun, J., Burmeister, H., Ott, I., Romero-Canelón, I., and Turel, I., “Towards Identification of Essential Structural Elements of Organoruthenium(II)-Pyrithionato Complexes for Anticancer Activity,” *Chemistry – A European Journal*, V. 25, No. 62, 2019, pp. 14169–14182.
57. Kladnik, J., Coverdale, J. P. C., Kljun, J., Burmeister, H., Lippman, P., Ellis, F. G., Jones, A. M., Ott, I., Romero-Canelón, I., and Turel, I., “Organoruthenium Complexes with Benzo-Fused Pyrithiones Overcome Platinum Resistance in Ovarian Cancer Cells,” *Cancers*, V. 13, No. 10, 2021.
58. He, L., Huang, Y., Zhu, H., Pang, G., Zheng, W., Wong, Y.-S., and Chen, T., “Cancer-Targeted Monodisperse Mesoporous Silica Nanoparticles as Carrier of Ruthenium Polypyridyl Complexes to Enhance Theranostic Effects,” *Advanced Functional Materials*, V. 24, No. 19, 2014, pp. 2754–2763.
59. Mladenović, M., Morgan, I., Ilić, N., Saoud, M., Pergal, M. V., Kaluđerović, G. N., and Knežević, N. Ž., “pH-Responsive Release of Ruthenium Metallotherapeutics from Mesoporous Silica-Based Nanocarriers,” *Pharmaceutics*, V. 13, No. 4, 2021.
60. Cooper, M. S., Heaney, H., Newbold, A. J., and Sanderson, W. R., “Oxidation Reactions Using Urea-Hydrogen Peroxide; A Safe Alternative to Anhydrous Hydrogen Peroxide,” *Synlett*, V. 1990, No. 09, 1990, pp. 533–535.

61. Kladnik, J., “Synthesis and biological activity of coordination compounds of pyrithione analogues,” University of Ljubljana, Faculty of Chemistry and Chemical Technology, Ljubljana, 2020.
62. Friebolin, H., “Ein- und zweidimensionale NMR-Spektroskopie: Eine Einführung,” 5. Auflage, Wiley-VCH, Weinheim, 2013, 1452 pp.
63. Hosangadi, B. D., and Dave, R. H., “An efficient general method for esterification of aromatic carboxylic acids,” *Tetrahedron Letters*, V. 37, No. 35, 1996, pp. 6375–6378.
64. Tao, Z., Toms, B., Goodisman, J., and Asefa, T., “Mesoporous silica microparticles enhance the cytotoxicity of anticancer platinum drugs,” *ACS Nano*, V. 4, No. 2, 2010, pp. 789–794.
65. Thommes, M., Kaneko, K., Neimark, A. V., Olivier, J. P., Rodriguez-Reinoso, F., Rouquerol, J., and Sing, K. S., “Physisorption of gases, with special reference to the evaluation of surface area and pore size distribution (IUPAC Technical Report),” *Pure and Applied Chemistry*, V. 87, 9-10, 2015, pp. 1051–1069.

6 Appendix

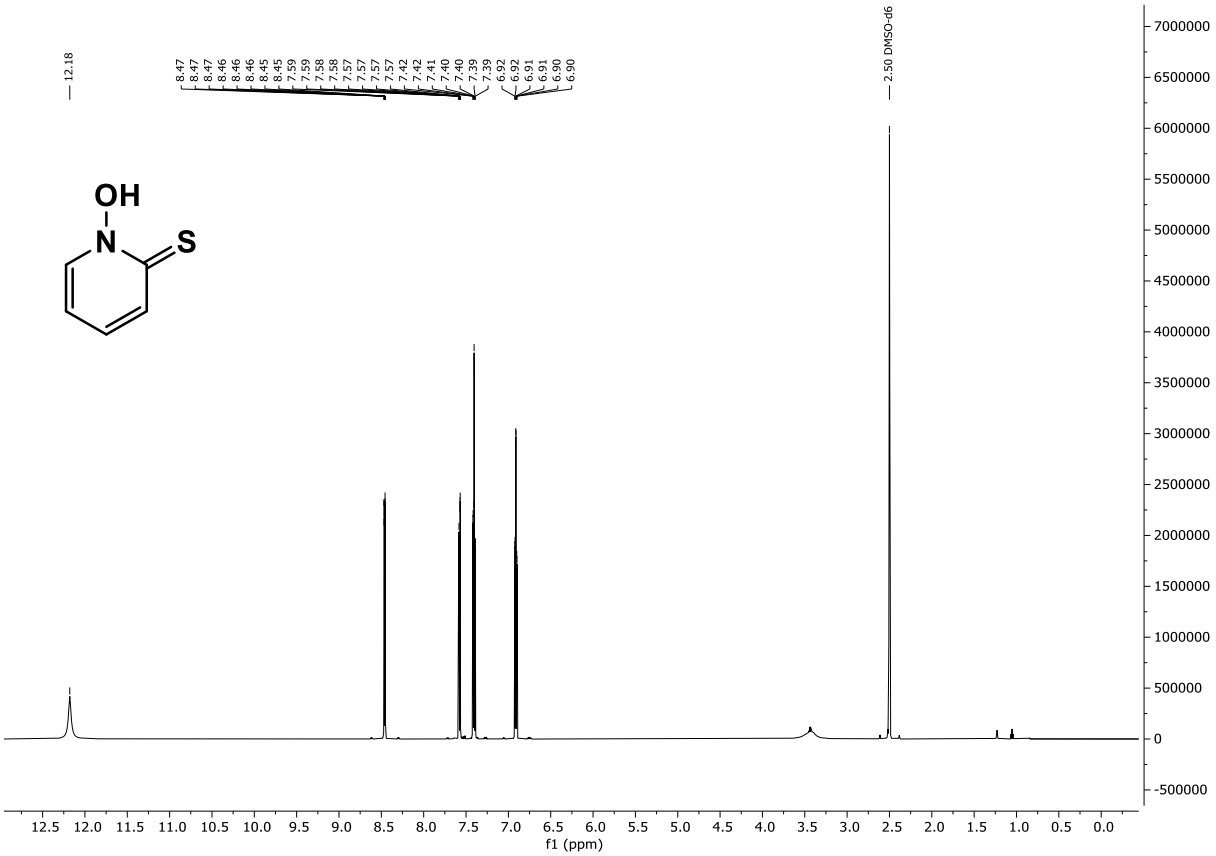

*Figure A1: ^{1}H NMR spectrum of pyrithione (**HL1**); in DMSO-$_{d6}$ (600 MHz)*

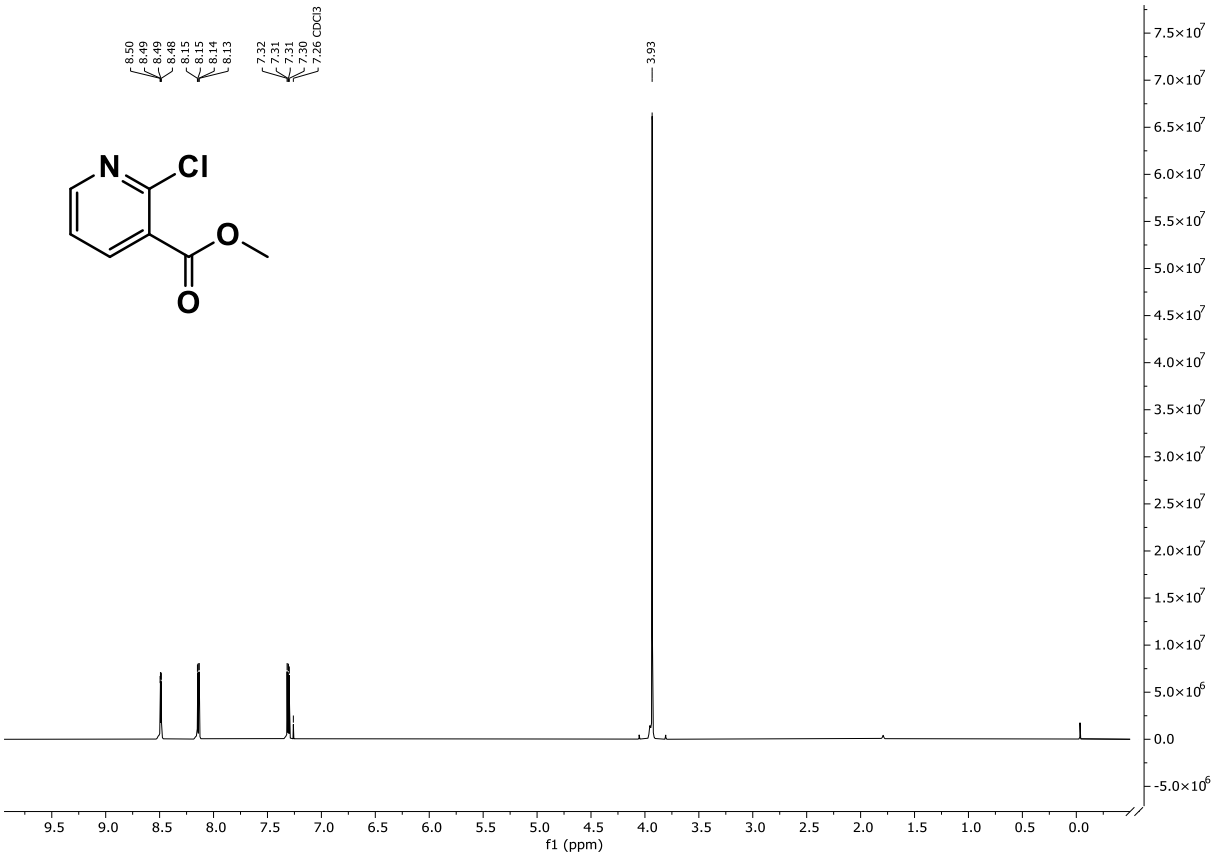

Figure A2: ^{1}H NMR spectrum of M2CN; in $CDCl_3$ (600 MHz)

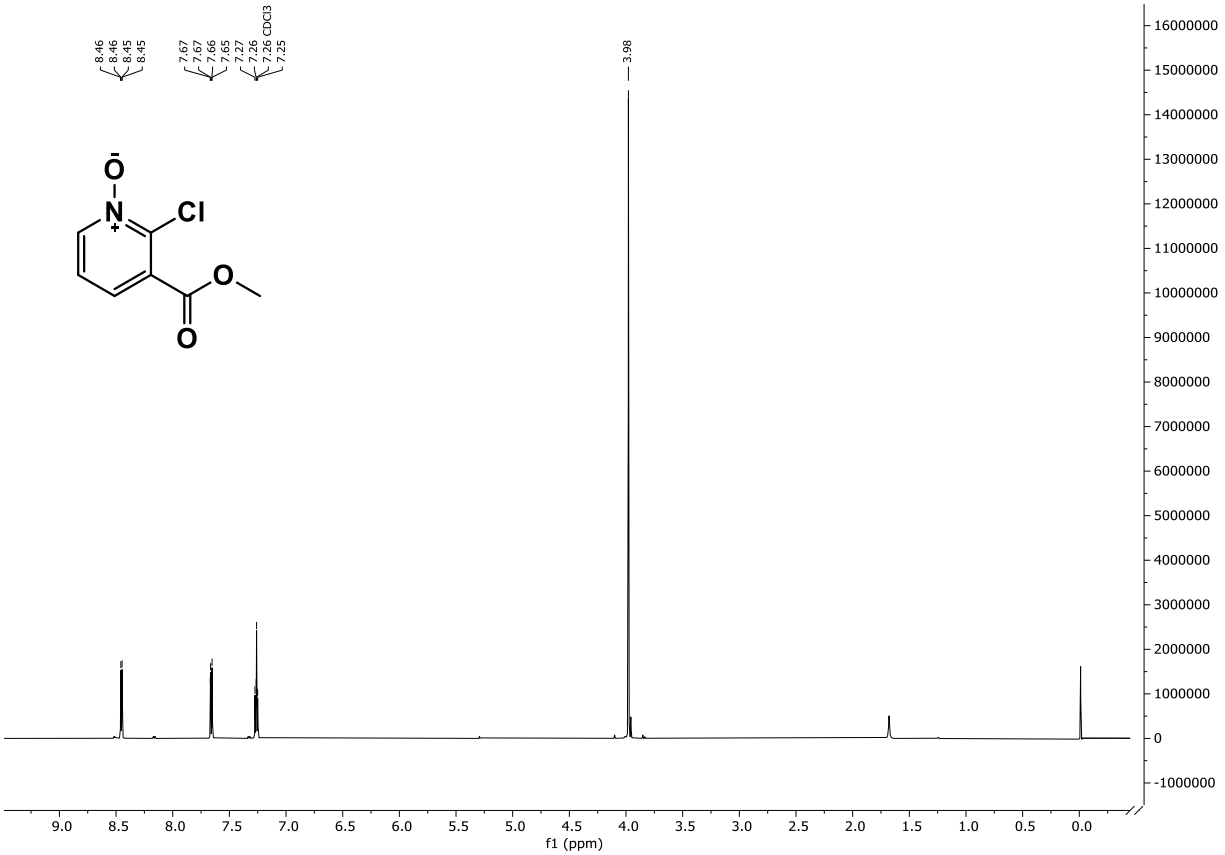

*Figure A3: ^{1}H NMR of **I1**; in $CDCl_3$ (600 MHz)*

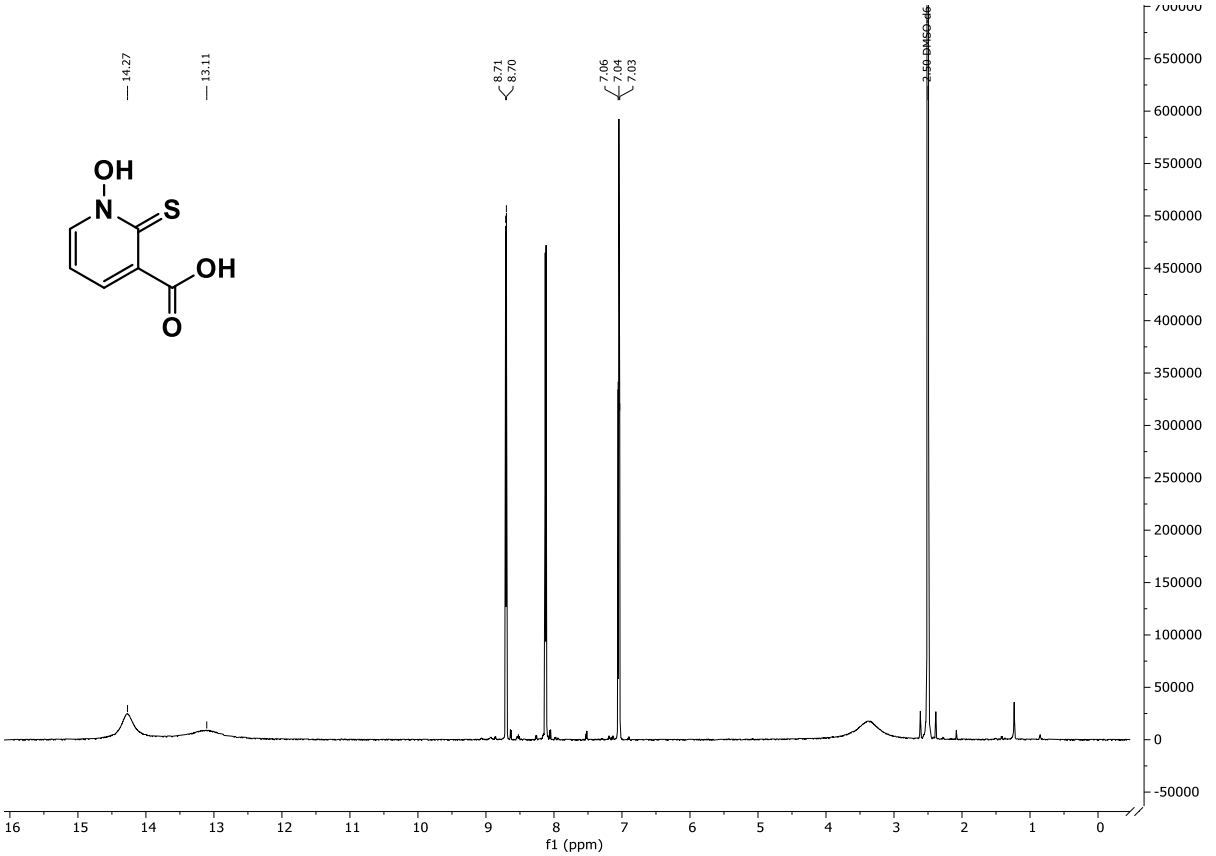

*Figure A4: ^{1}H NMR spectrum of **H_2L2**, in DMSO-d_6 (600 MHz)*

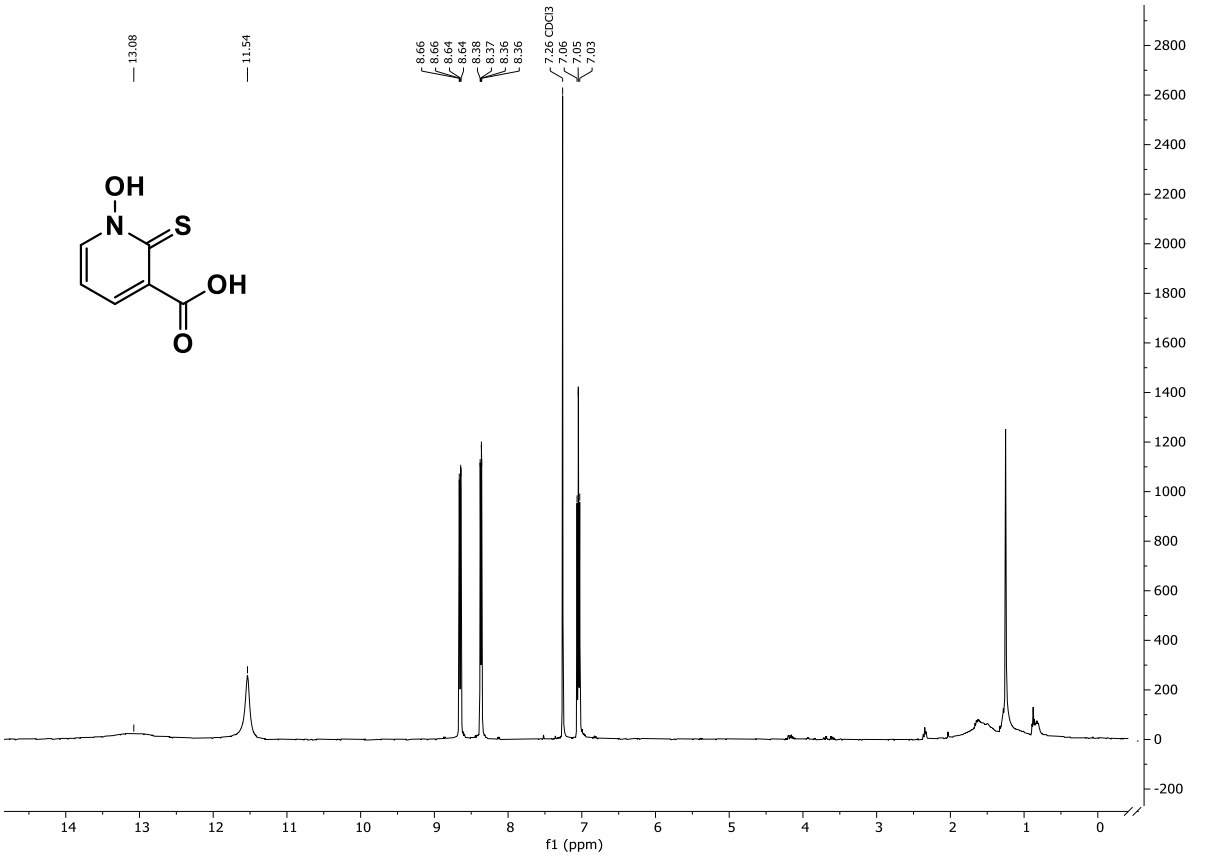

*Figure A5: ^{1}H NMR spectrum of **H_2L2**, in $CDCl_3$ (400 MHz)*

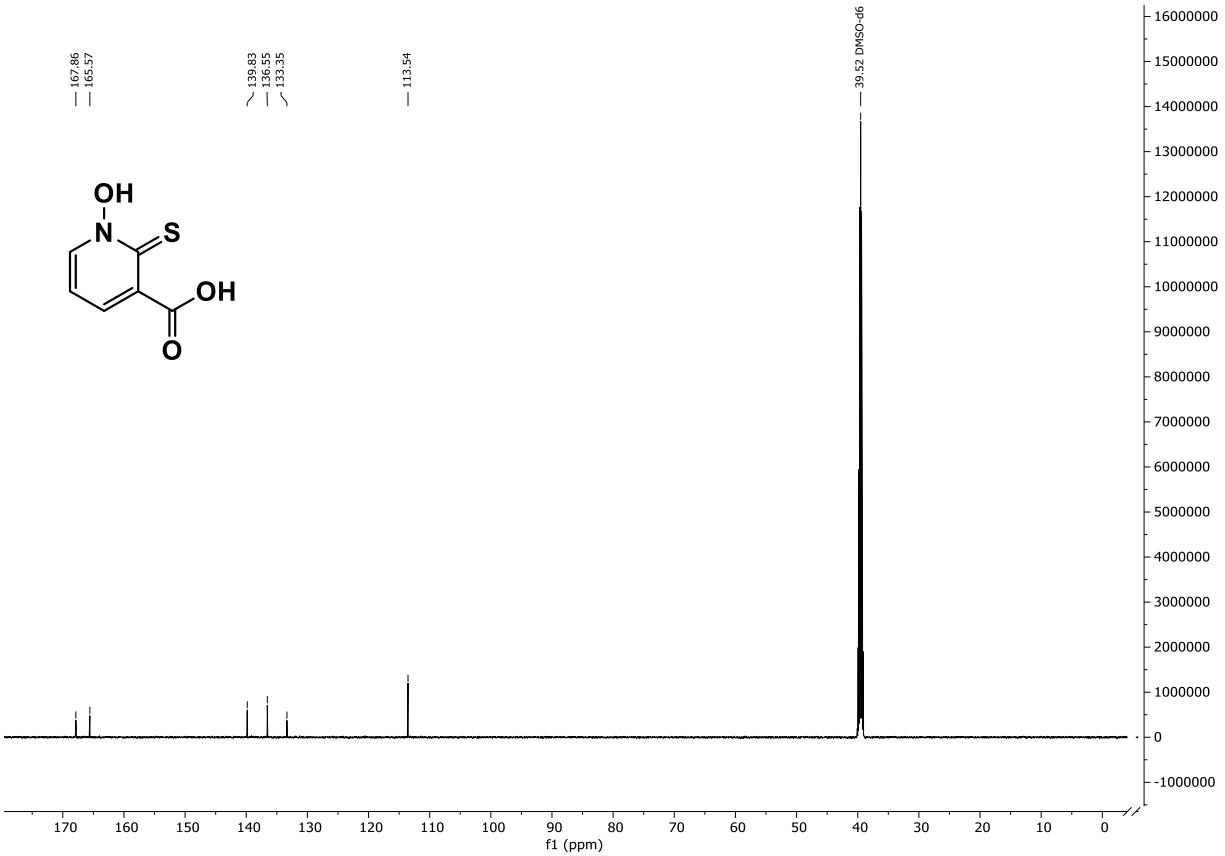

*Figure A6: ^{13}C NMR spectrum of **H_2L2**, in DMSO-d_6 (600 MHz)*

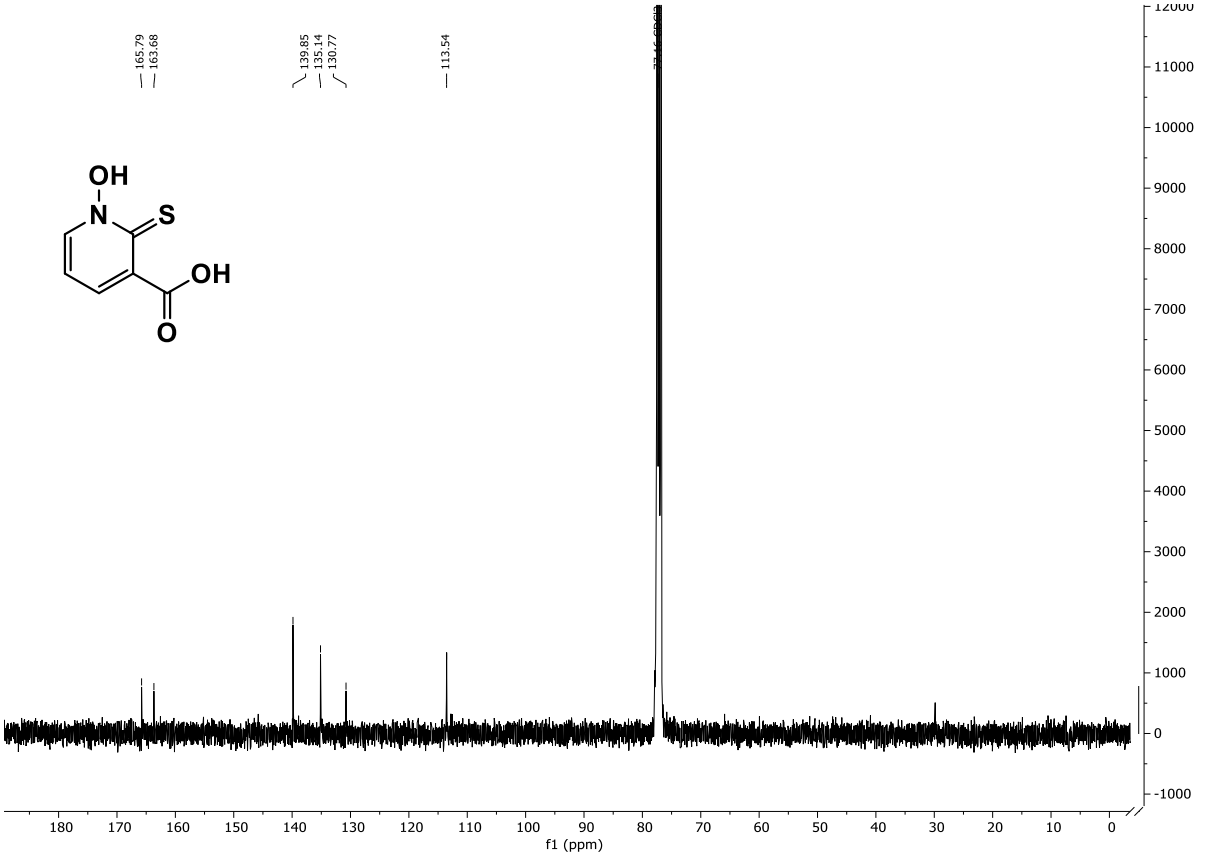

*Figure A7: ^{13}C NMR spectrum of **H_2L2**, in $CDCl_3$ (400 MHz)*

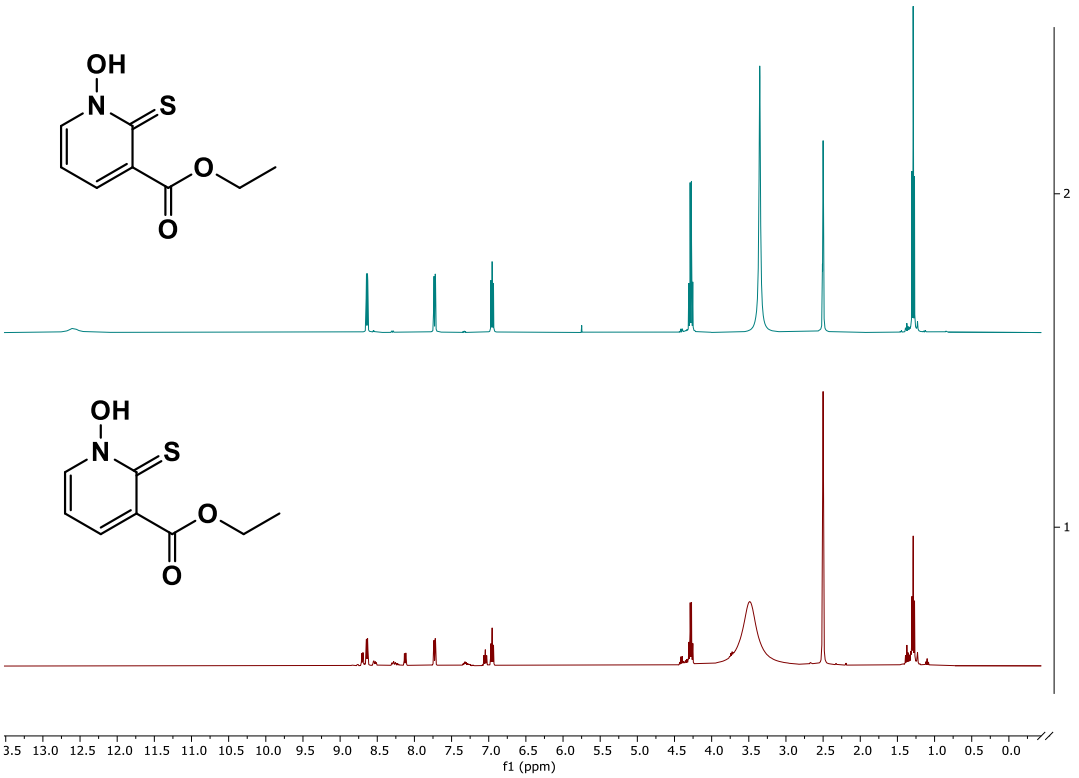

*Figure A8 : [1]H NMR spectrum of **HL3** before (lower) and after (upper) clean-up using 2% MeOH/DCM; in DMSO-d_6 (400 MHz)*

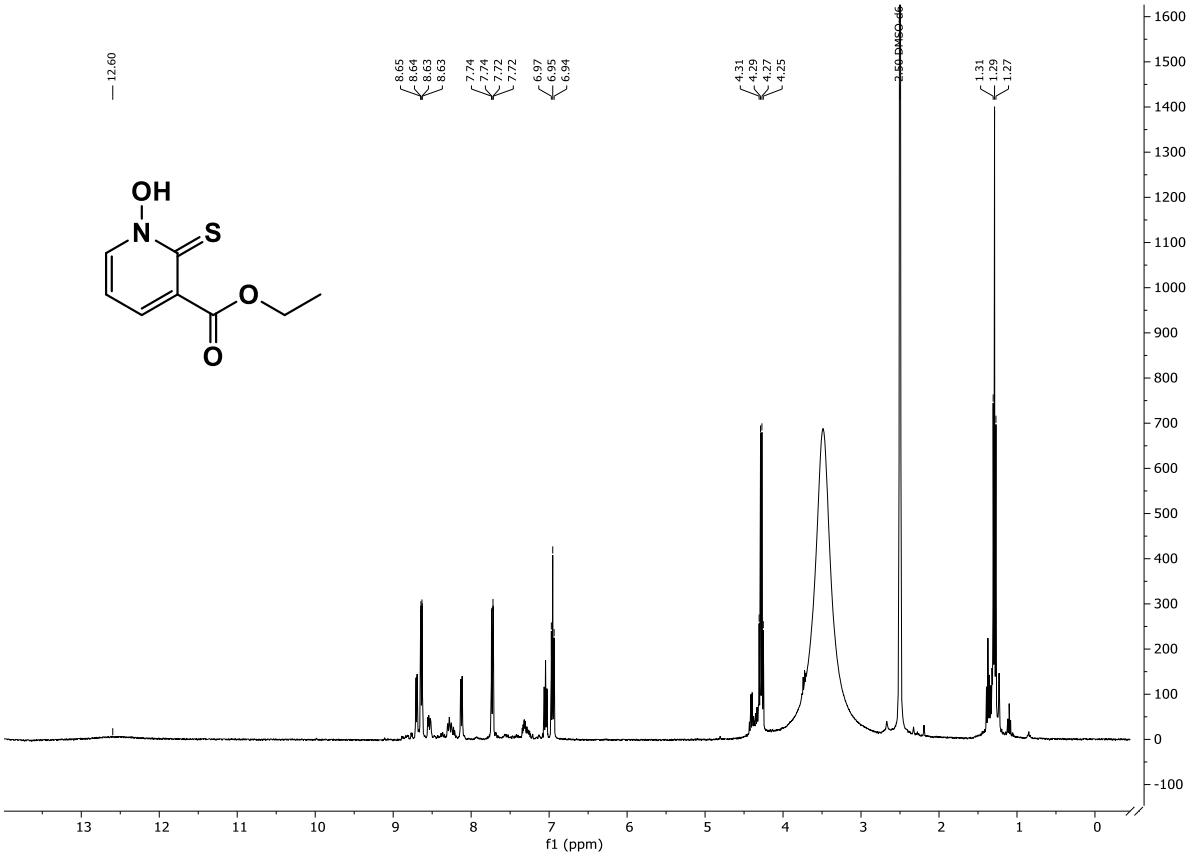

*Figure A9: [1]H NMR spectrum of **HL3** before clean-up with 2% MeOH/DCM; in DMSO-d_6 (400 MHz)*

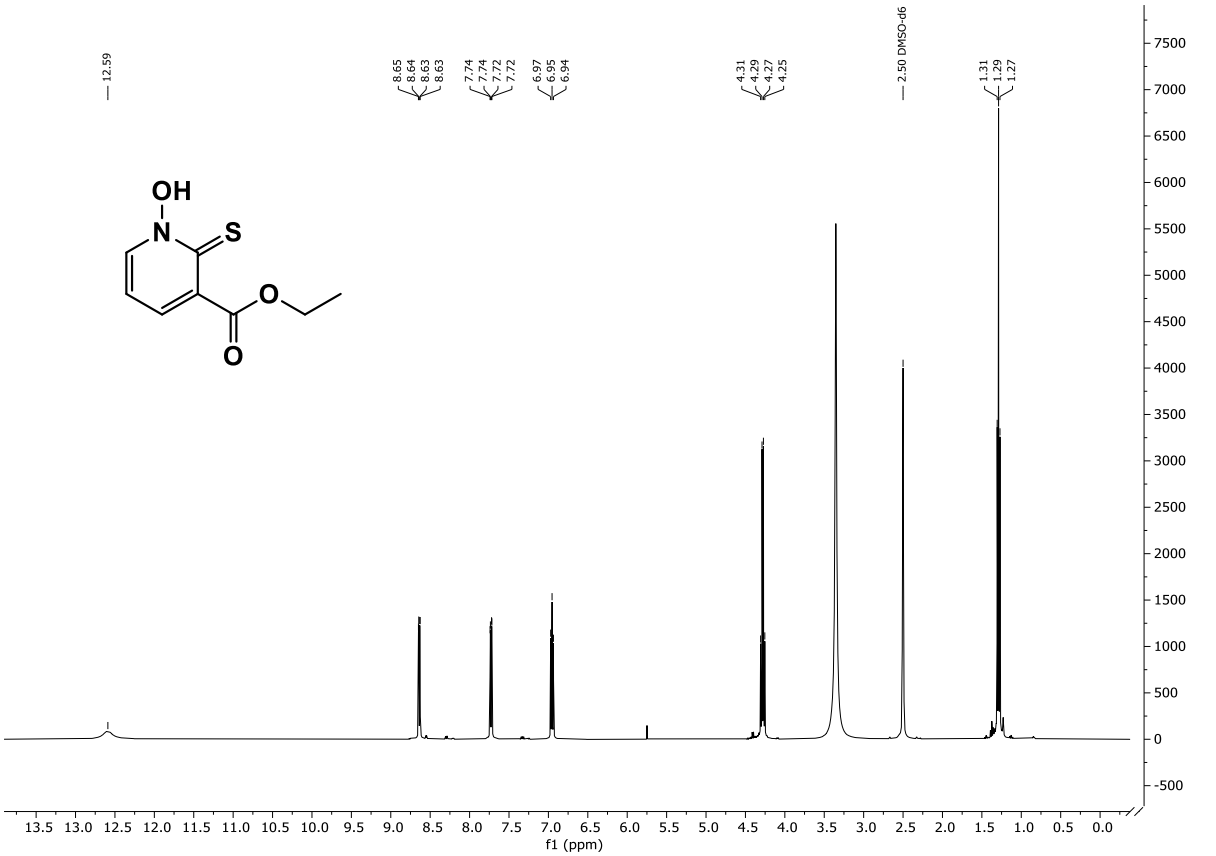

*Figure A10: ^{1}H NMR spectrum of **HL3** after cleanup with 2% MeOH/DCM; in DMSO-d_6 (400 MHz)*

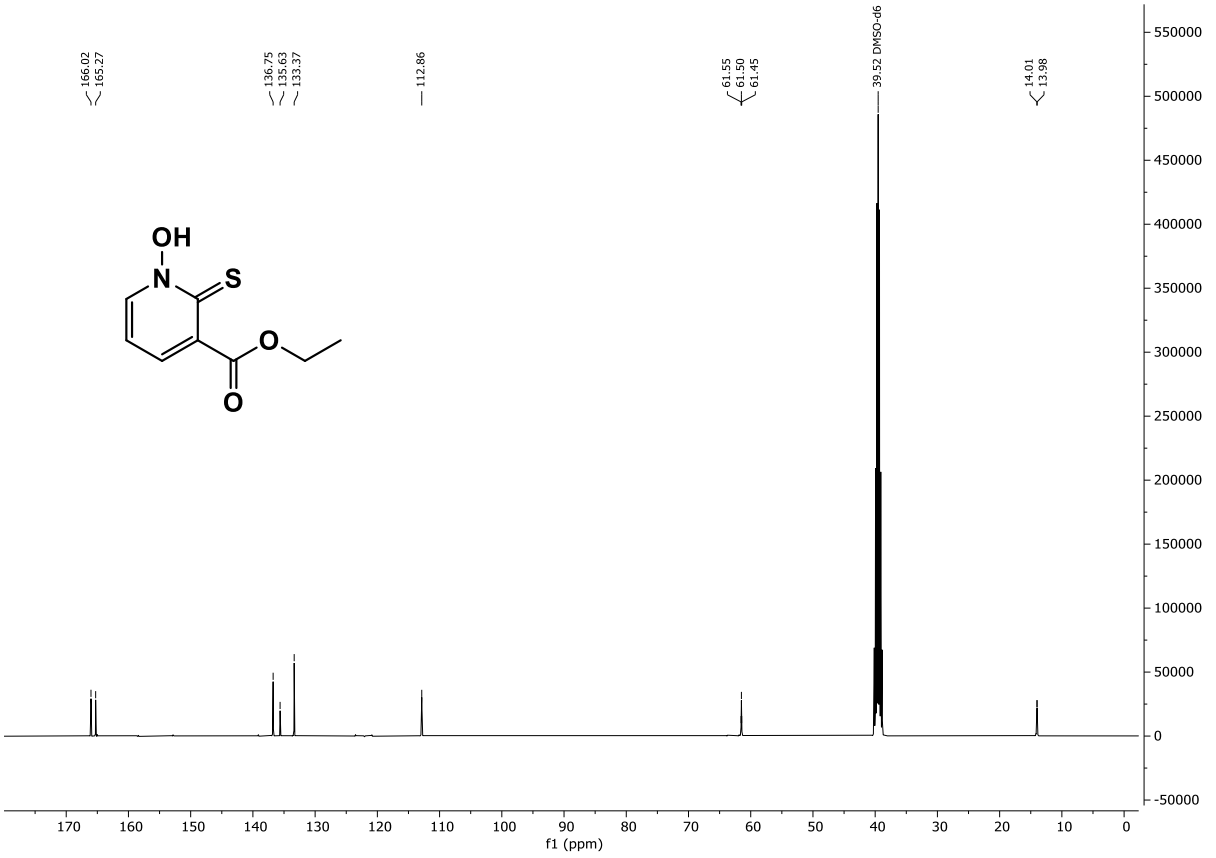

*Figure A11: ^{13}C NMR of **L3**; in DMSO-d_6 (400 MHz)*

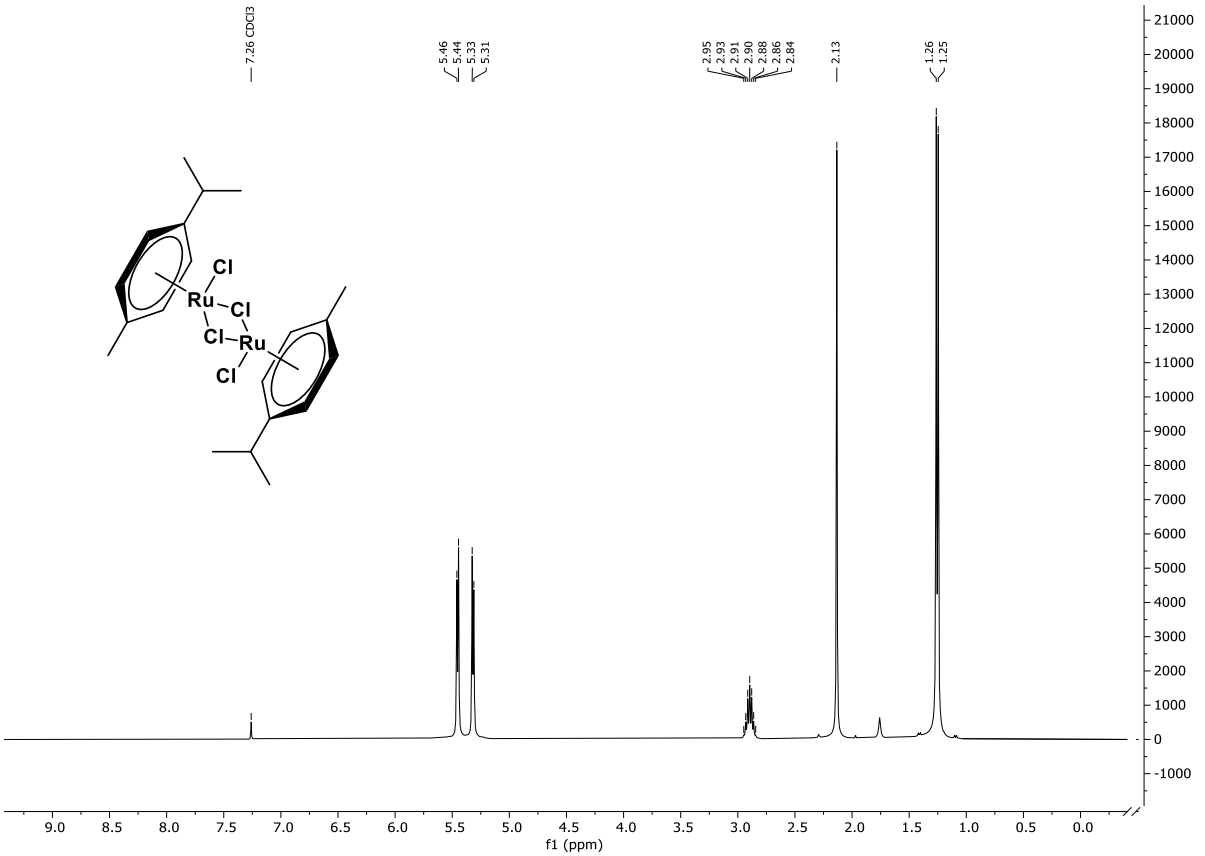

Figure A12: ^{1}H NMR spectrum of [{Ru(p-cymene)Cl$_2$}$_2$]; in CDCl$_3$ (400 MHz)

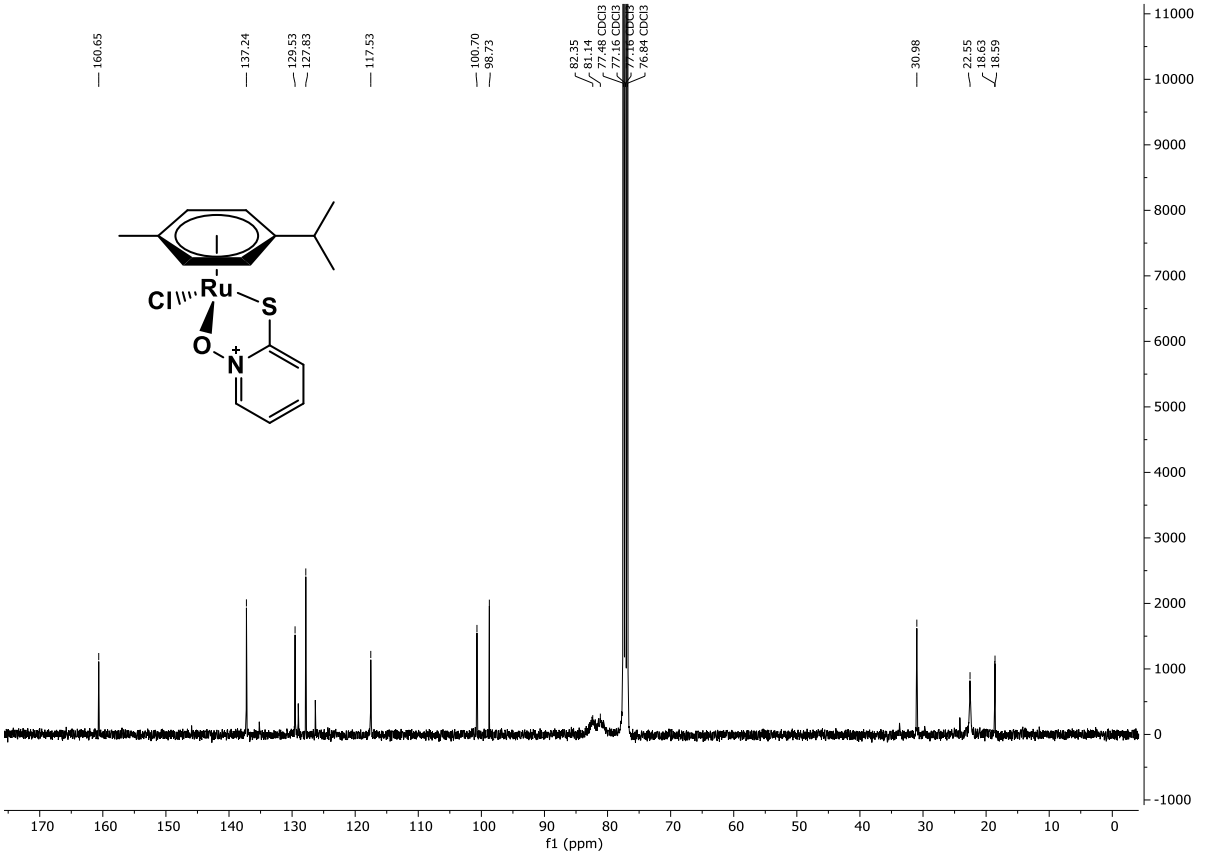

*Figure A13: ^{13}C NMR spectrum of **1**; in CDCl$_3$ (400 MHz)*

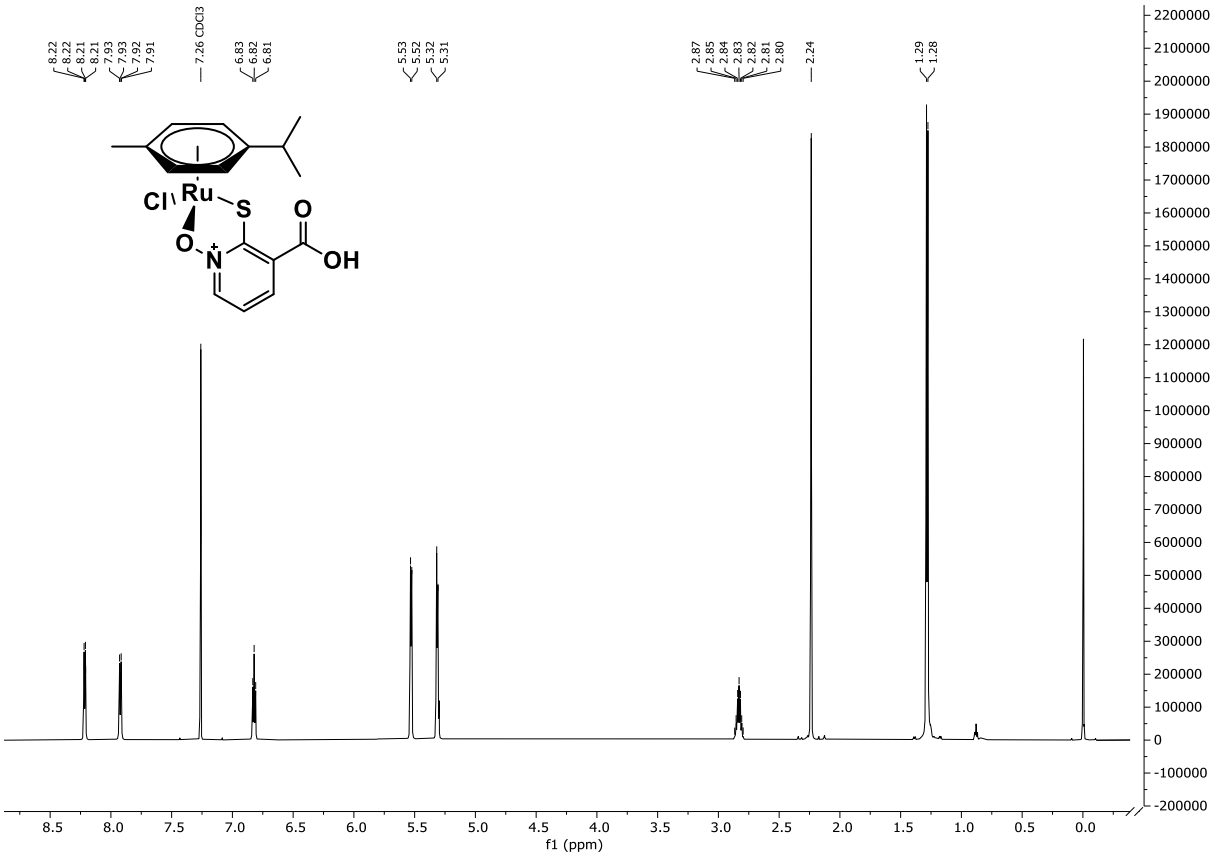

*Figure A14: ^{1}H NMR spectrum of **2**; in $CDCl_3$ (400 MHz)*

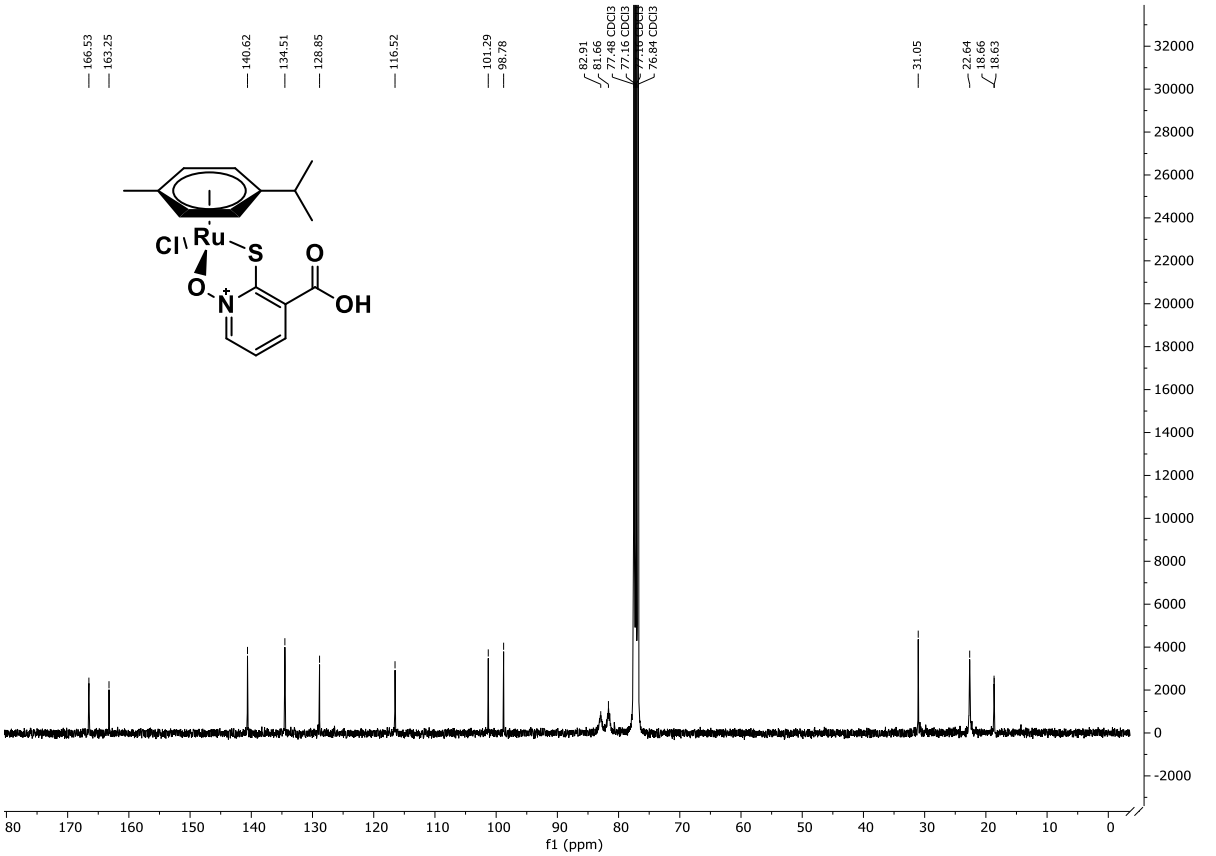

*Figure A15: ^{13}C NMR spectrum of **2**; in $CDCl_3$ (400 MHz)*

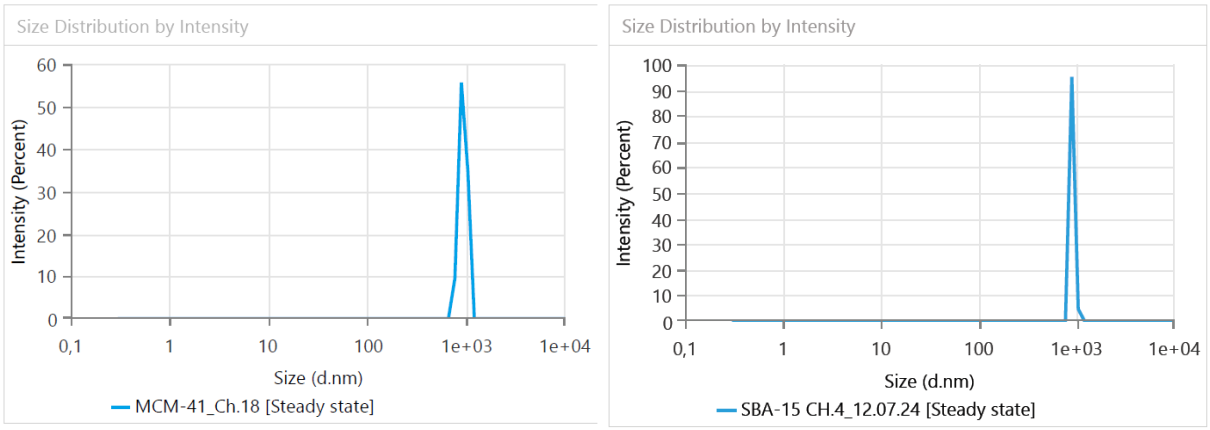

Figure A16: DLS-size measurements of MCM-41 (left) and SBA-15 (right)

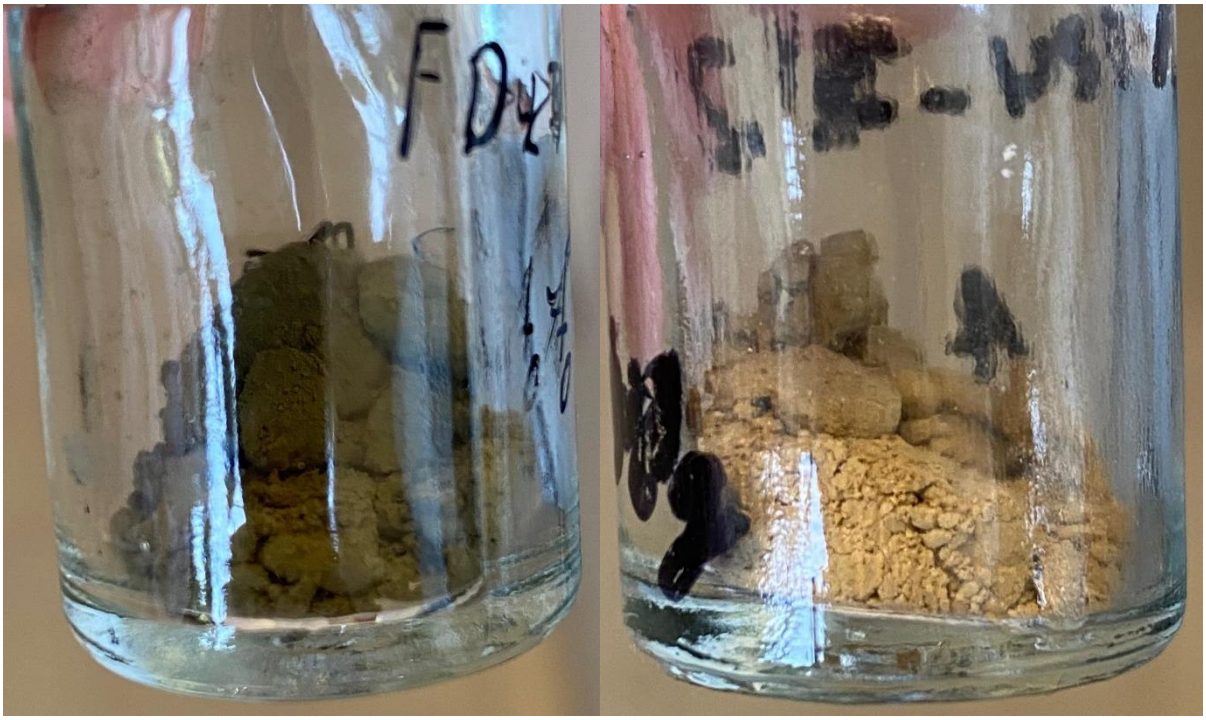

Figure A17: loaded MSNs using immobilization at 80 °C|48 h (left) and 20 °C|96 h (right)